A&A 660, A84 (2022)
https://doi.org/10.1051/0004-6361/202142515

Astronomy & Astrophysics

The first widespread solar energetic particle event of solar cycle 25 on 2020 November 29

Shock wave properties and the wide distribution of solar energetic particles[★]

A. Kouloumvakos[1], R. Y. Kwon[2,3], L. Rodríguez-García[4], D. Lario[5], N. Dresing[6], E. K. J. Kilpua[7], R. Vainio[6], T. Török[8], I. Plotnikov[1], A. P. Rouillard[1], C. Downs[8], J. A. Linker[8], O. E. Malandraki[9], R. F. Pinto[1,10], P. Riley[8], and R. C. Allen[11]

[1] IRAP, Université Toulouse III – Paul Sabatier, CNRS, CNES, Toulouse, France
e-mail: `athkouloumvakos@gmail.com`
[2] Korea Astronomy and Space Science Institute, Daejeon 34055, Republic of Korea
[3] Science and Technology Policy Institute, Korea Space Policy Research Center, Sejong 30147, Republic of Korea
[4] Universidad de Alcalá, Space Research Group, Alcalá de Henares, Madrid, Spain
[5] NASA, Goddard Space Flight Center, Heliophysics Science Division, Greenbelt 20771, USA
[6] Department of Physics and Astronomy, University of Turku, Turku, Finland
[7] Department of Physics, University of Helsinki, Helsinki, Finland
[8] Predictive Science Inc., 9990 Mesa Rim Rd., Ste. 170, San Diego 92121, USA
[9] National Observatory of Athens, Institute for Astronomy, Astrophysics, Space Applications and Remote Sensing, Athens, Greece
[10] Dept. d'Astrophysique/AIM, CEA/IRFU, CNRS/INSU, Université Paris-Saclay, 91191 Gif-sur-Yvette Cedex, France
[11] Johns Hopkins Applied Physics Lab, Laurel 20723, USA

Received 22 October 2021 / Accepted 22 January 2022

ABSTRACT

Context. On 2020 November 29, an eruptive event occurred in an active region located behind the eastern solar limb as seen from Earth. The event consisted of an M4.4 class flare, a coronal mass ejection, an extreme ultraviolet (EUV) wave, and a white-light (WL) shock wave. The eruption gave rise to the first widespread solar energetic particle (SEP) event of solar cycle 25, which was observed at four widely separated heliospheric locations (~230°).

Aims. Our aim is to better understand the source of this widespread SEP event, examine the role of the coronal shock wave in the wide distribution of SEPs, and investigate the shock wave properties at the field lines magnetically connected to the spacecraft.

Methods. Using EUV and WL data, we reconstructed the global three-dimensional structure of the shock in the corona and computed its kinematics. We determined the magnetic field configurations in the corona and interplanetary space, inferred the magnetic connectivity of the spacecraft with the shock surface, and derived the evolution of the shock parameters at the connecting field lines.

Results. Remote sensing observations show formation of the coronal shock wave occurring early during the eruption, and its rapid propagation to distant locations. The results of the shock wave modelling show multiple regions where a strong shock has formed and efficient particle acceleration is expected to take place. The pressure/shock wave is magnetically connected to all spacecraft locations before or during the estimated SEP release times. The release of the observed near-relativistic electrons occurs predominantly close to the time when the pressure/shock wave connects to the magnetic field lines or when the shock wave becomes supercritical, whereas the proton release is significantly delayed with respect to the time when the shock wave becomes supercritical, with the only exception being the proton release at the Parker Solar Probe.

Conclusions. Our results suggest that the shock wave plays an important role in the spread of SEPs. Supercritical shock regions are connected to most of the spacecraft. The particle increase at Earth, which is barely connected to the wave, also suggests that the cross-field transport cannot be ignored. The release of energetic electrons seems to occur close to the time when the shock wave connects to, or becomes supercritical at, the field lines connecting to the spacecraft. Energetic protons are released with a time-delay relative to the time when the pressure/shock wave connects to the spacecraft locations. We attribute this delay to the time that it takes for the shock wave to accelerate protons efficiently.

Key words. Sun: general – Sun: particle emission – Sun: coronal mass ejections (CMEs) – shock waves

1. Introduction

Solar cycle 24 was one of the weakest solar cycles of the last ~100 yr, with a peak sunspot number lower than in prior solar cycles (e.g., Nandy 2021). Solar activity has declined over the past four solar cycles (from 21 to 24). M- and X-class flare rates, as well as geomagnetic activity, were also remarkably low compared to previous solar cycles (Gopalswamy et al. 2015a). The rate of very-high-energy solar energetic particle events (SEPs; Reames 2015) was low as well, with only two ground-level enhancements (GLEs), but with many individual SEP events observed at lower energies (e.g., Richardson et al. 2014; Gopalswamy et al. 2015b; Paassilta et al. 2018).

[★] Movie associated to Fig. 2 is available at `https://www.aanda.org`

Remote-sensing and in situ observations by widely separated spacecraft, including the spacecraft of the Solar TErrestrial RElations Observatory (STEREO; Kaiser et al. 2008) and near-Earth spacecraft, have allowed us to study the origins of SEP events, their wide distribution in the heliosphere (e.g., Richardson et al. 2014), and the role of coronal mass ejections (CMEs; Webb & Howard 2012) and shock waves in the acceleration and release of energetic particles with a better perspective (e.g., Desai & Giacalone 2016; Lario et al. 2017b; Anastasiadis et al. 2019; Vlahos et al. 2019; Zhang et al. 2021). From a space-weather perspective, we are interested in not only explaining the intensity of SEP events but also their wide extension in the heliosphere (e.g., Klein & Dalla 2017). These large and widespread SEP events are often associated with fast and wide CMEs driving coronal and interplanetary shock waves that expand over large longitudinal spans (e.g., Rodríguez-García et al. 2021). In some events, observations suggest that the shock wave can even encompass the Sun and be observed as global waves propagating above the solar surface (e.g., Warmuth 2015; Downs et al. 2021).

In principle, shock waves driven by fast and wide CMEs and propagating over large longitudinal distances can facilitate particle acceleration and injection of SEPs over a broad range of longitudes (Lario et al. 2016, 2017a). For example, the case study of the multi-spacecraft SEP event on 2011 March 21 by Rouillard et al. (2012) showed that the SEP event, caused by a fast and wide CME, and the particle onset times were consistent with the time needed for the coronal shock wave to propagate to the locations of the magnetic footpoints connected to the observing spacecraft. Additionally, SEP transport processes can contribute to the wide distribution of SEPs (e.g., Dalla et al. 2003; Dröge et al. 2010; Laitinen et al. 2013). In this case, the particles originating from either a narrow or an extended source could propagate to distant locations in the corona or interplanetary space, for example by diffusion perpendicular to the magnetic field lines, or along meandering field lines, and thus contribute to the extent of the widespread SEP events (Laitinen et al. 2016). Both processes (CME and shock wave, or transport processes) can in principle be responsible for the observed delays between the onset times of the associated type III radio emissions and the SEP release times (e.g., Kouloumvakos et al. 2015).

It has been suggested that the expansion of extreme ultraviolet (EUV) waves close to the solar corona, which are thought to trace the lateral propagation of CME-driven shock waves in the corona (e.g., Patsourakos et al. 2009; Patsourakos & Vourlidas 2012), might be related to the particle acceleration and injection over a broad range of heliolongitudes (e.g., Torsti et al. 1999; Malandraki et al. 2009; Kozarev et al. 2015; Kouloumvakos et al. 2020b). From a statistical analysis of 12 energetic proton events, Park et al. (2013) show that the EUV arrival times were significantly associated with the onset times of the SEP events. On the other hand, Miteva et al. (2014) studied a large number of EUV waves and show that the EUV wave expansion speeds are too low to explain the release times of (near-)relativistic electrons.

More recently, it has also been suggested that halo fronts, referred to as halo CMEs, are the observations of spherically formed shock waves, rather than a simple projection of expanding CME ejecta (Kwon et al. 2015). EUV waves are the ground track of the spherical halo-shaped coronal shock waves propagating in the higher solar corona, and thus actual shock waves can propagate much further than the EUV waves (Kwon et al. 2013). In two case studies of the widespread SEP events observed on 2013 April 11 and 2014 February 25, Lario et al. (2014, 2016) show that the halo-shaped coronal shock waves are responsible for the release of SEPs, regardless of whether the EUV waves are observed or not. For the 2011 November 3 event, which showed an unusually rapid onset at widespread spacecraft, Prise et al. (2014) concluded that the shock wave associated with the CME at larger heights in the middle corona was responsible for the large longitudinal expansion of the SEP event (also Kouloumvakos et al. 2016, for the 2012 March 7 SEP event). For the same event, Gómez-Herrero et al. (2015) showed strong anisotropies that disfavoured perpendicular transport in the interplanetary medium and the authors suggested that the SEPs spread quickly close to the Sun.

Therefore, what determines the longitudinal spread of SEP events in some events may not be the EUV wave extent close to the solar surface but the shock-wave propagation at greater heights in the middle corona. For example, as Zhu et al. (2018) show from the analysis of the 2012 January 27 event, the shock propagation can be faster higher in the corona than close to the solar surface (EUV wave) for some events (Kwon et al. 2013). This is also the theoretical expectation, because the Alfvén speed increases as a function of height up to about 2–4 solar radii above quiet-Sun regions (Mann et al. 2003; Warmuth & Mann 2005). On the other hand, low values of the first-order anisotropy observed in some widespread energetic electron events suggest that cross-field transport in the interplanetary medium could also play an important role (e.g., Dresing et al. 2014). For example, in the case study of the 2010 January 17 widespread SEP event, Dresing et al. (2012) showed that interplanetary perpendicular diffusion transport processes account for this event. Close to the onset of the SEP event, SEP observations showed weak particle anisotropies and significant time-delays with respect to the parent solar eruption. In summary, previous studies showed that SEP events have a variety of characteristics (e.g., release times and particle anisotropies), meaning that it is more likely that a combination of multiple processes, including the CME-driven shock wave and SEP transport effects, contributes to the wide distribution of energetic particles seen in many SEP events (e.g., Rodríguez-García et al. 2021).

In this paper, we study the first widespread SEP event of solar cycle 25 on 2020 November 29. The SEP event was observed by the recently launched solar missions Solar Orbiter (SolO; Müller et al. 2020) and Parker Solar Probe (PSP; Fox et al. 2016), and also by the STEREO-A and near-Earth spacecraft. These spacecraft were widely distributed in the heliosphere. Kollhoff et al. (2021) show that during this solar event, energetic particles spread over more than 230° in longitude. The large particle anisotropy observed at the onset of this event at SolO and STEREO-A (Kollhoff et al. 2021), together with the fact that the onset of the SEP event at PSP also exhibited field-aligned antisunward anisotropies (e.g., Fig. 14 in Cohen et al. 2021), suggest that particles were possibly injected over a wide longitudinal range close to the Sun. Kollhoff et al. (2021) also show that the EUV wave arrival times at the corresponding field-line footpoints do not clearly correlate with the release times of the energetic particles for each spacecraft. In this study, we analyse EUV and white-light (WL) coronagraph observations in detail, model the observed shock wave, and examine the magnetic connectivity of the different spacecraft with this shock wave to investigate the role of the shock in the origin of the widespread SEP event for each observer. We also examine the delays between the electron and proton release times as a function of the connection angle of each observing spacecraft with respect to the site of the solar event.

The paper is structured as follows. In Sect. 2 we give an overview of the eruption and the SEP observations, and analyse the shock wave seen in the EUV and WL observations in detail. In Sect. 3, we model the shock wave properties in three dimensions (3D). We also examine the magnetic field configurations (coronal and interplanetary) to estimate the magnetic connectivity with each spacecraft. In Sect. 4, we examine the evolution of the shock parameters at the field lines magnetically connected to the spacecraft and relate them with the particle observations. Finally, we discuss our results and present our conclusions in Sects. 5 and 6.

2. Observations

2.1. Overview

On 2020 November 29, an M4.4 class flare occurred at NOAA active region (AR) 12790 located behind the east limb as seen from Earth. According to the GOES soft X-ray (1–8 Å) flux, the flare started at around 12:35 UT and peaked at 13:11 UT. The solar flare was located at E98S23 (in Stonyhurst heliographic (HGS) coordinates) and was associated with a CME with a speed of ~1780 km s^{-1} at the leading edge and a width[1] of ~74° (Nieves-Chinchilla et al. 2022). A shock wave in WL was observed as a fainter front around the bright CME in the extended corona, as often referred to as the halo front, while an EUV wave propagated in the low corona. Associated with the event, a type II radio burst and multiple type III radio bursts were observed. We further discuss these remote-sensing observations in Sect. 2.3.

Prior to the occurrence of this event, the solar activity was not at a high level, in accordance with the relatively quiet solar conditions at the beginning of solar cycle 25. Only a few weak flares (≤C-class) and slow CMEs were observed during the days before the 2020 November 29 event. Specifically, two CMEs occurred on 2020 November 24, and one on 2020 November 26. All three CMEs were significantly slower than the one on 2020 November 29. Because these CMEs could have affected the interplanetary medium prior to our SEP event, we reconstructed these CMEs and injected them into a 3D magnetohydrodynamic (MHD) simulation in order to explore the large-scale interplanetary magnetic field (IMF) configuration and estimate the magnetic connectivity of each spacecraft (Sect. 3.2.1).

2.2. The widespread SEP event

The solar eruption and CME on 2020 November 29 caused the first widespread SEP event of solar cycle 25. Kollhoff et al. (2021) showed that the associated high-energy protons and electrons rapidly filled the inner heliosphere following the solar event. Energetic particle observations by SolO, PSP, STEREO-A, and multiple missions near the Sun-Earth Lagrangian L1 point showed increases of relativistic electrons as well as high-energy protons with energies >50 MeV. In Fig. 1 we show the locations of the different spacecraft during the event, as seen from north of the ecliptic. All spacecraft were located at heliocentric radial distances close to 1 au, except for SolO and PSP, which were located at 0.88 au and 0.81 au, respectively. The spacecraft were widely separated, spanning almost 230° in longitude during the event (see Fig. 1) and the eruption was headed towards PSP which was almost aligned with the propagation direction of the CME. In Fig. 1 we show the nominal Parker spiral magnetic field lines connecting each spacecraft with the Sun using the solar wind speeds measured by each spacecraft as given in Table 1. Those were calculated using one-hour averaged measurements near the SEP event onset time, except for SolO and PSP because the solar wind analyser on this spacecraft was not operational and a speed from an ENLIL simulation (see Sect. 3.2) has been assumed. The magnetic footpoints of PSP and SolO at the Sun were the closest to the flare location.

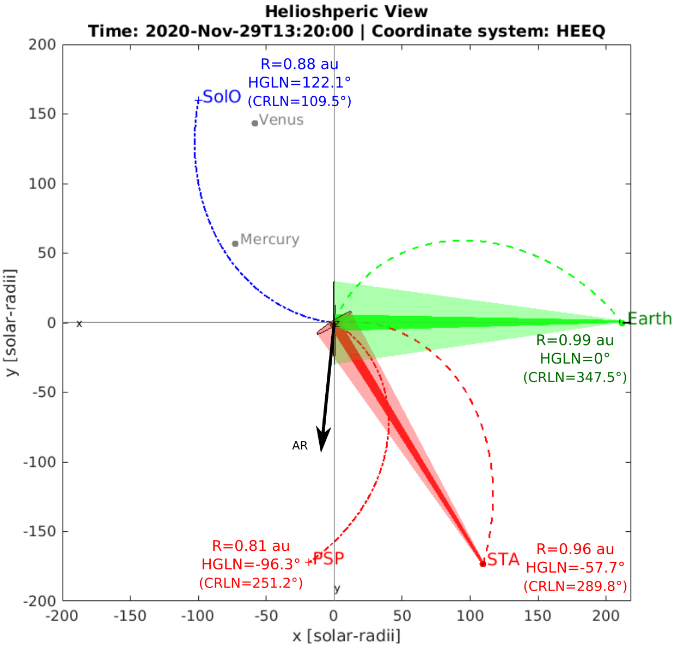

Fig. 1. View of the ecliptic plane from solar north showing the locations of the Sun, Earth, PSP, SolO, and STEREO-A in the HEEQ coordinate system on 2020 November 29 at 13:20 UT. The fields of view of STEREO-A/COR1 and COR2 and SOHO/LASCO-C2 and C3 are depicted as shaded areas in red and green, respectively. Positions are given by the labels next to each spacecraft or planet marker. The location of the parent AR12790 is indicated by the black arrow. The Parker spirals for the solar wind speed measured by each spacecraft at the time of the eruption are shown by the lines connecting the spacecraft to the solar surface.

The spacecraft locations during this solar event provide the opportunity to study this widespread SEP event from four vantage points. As discussed in Kollhoff et al. (2021) the large particle anisotropies observed by SolO and STEREO-A at the onset of the SEP event suggest that the energetic particles were injected over a wide longitudinal range close to the Sun (e.g., ≥180° for SolO–STEREO-A longitudinal separation). On the other hand, the low values of the first-order anisotropy observed by the Wind spacecraft suggest that diffusive propagation processes (e.g., cross-field transport) were likely involved in the particle transport to this location. The highest particle intensities were measured by PSP (e.g., see Fig. 1 in Kollhoff et al. 2021), for which the nominal magnetic connection was the closest to the AR 12790. The longitudinal angular separation ΔLon between the flare site and the nominal magnetic footpoint of PSP was about ~69°. In contrast, moderate SEP intensities were measured by SolO and STEREO-A whose nominal magnetic footpoints were quite distant from AR12790 (|ΔLon.| > 90°). Additionally, the analysis of the spectra and composition of the SEP event observed by PSP suggests that its characteristics are overall consistent with an event where the main SEP acceleration takes

---

[1] The CME width is based on Dumbović et al. (2019). It is the angular extent in the equatorial plane taking the CME tilt into account.

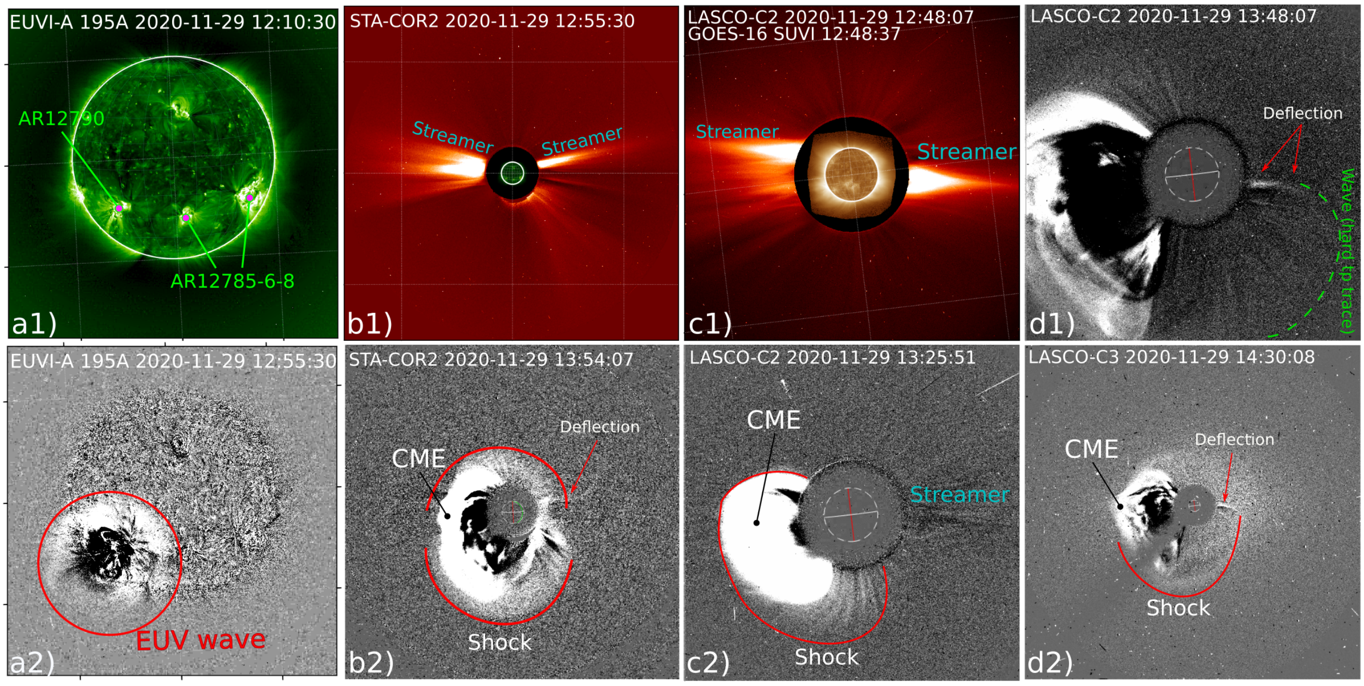

Fig. 2. Selected snapshots of EUV and WL coronagraphic observations before and during the 2020 November 29 event. *Panels a1, a2*: EUV observations from STEREO-A/EUVI at 195 Å: (*a1*) Image before the event where we mark the ARs of interest discussed in the text. (*a2*) Running-difference image during the event, with the EUV wave encircled. *Panels b–d*: coronagraphic observations from STEREO-A/COR2 and LASCO-C2, respectively; (*b1*) and (*c1*) are images before the event where we mark the location of streamers and (*b2*), (*c2*), and (*d*) are running-difference images during the event where we indicate the CME and we outline the location of the shock wave. Here we mark the locations where the shock interacted with the streamers and a deflection was observed. The associated movie is available online.

place at a CME-driven shock (Mason et al. 2021; Cohen et al. 2021).

2.3. Remote sensing observations (EUV, white-light)

Remote-sensing observations from Earth and STEREO-A provide a good view of the CME. The longitudinal separation of STEREO-A with respect to Earth was ~60°, offering a $\lesssim 240°$ longitudinal coverage from the two viewing points. The Sun Earth Connection Coronal and Heliospheric Investigation (SECCHI) instrument suite on board STEREO-A (Howard et al. 2008), consisting of an Extreme Ultraviolet Imager (EUVI), two WL coronagraphs (SECCHI/COR1 and COR2), and the Heliospheric Imagers (HI1-2), observed the CME from the low corona to interplanetary space. From this viewpoint, the CME was seen as a halo in coronagraphic images. From Earth, the CME was observed in WL by the Large Angle and Spectrometric Coronagraph Experiment (LASCO; Brueckner et al. 1995) on board SOHO and in EUV. Images were also taken by the Atmospheric Imaging Assembly (AIA) on board the Solar Dynamics Observatory (SDO; Lemen et al. 2012), and also by the Solar UltraViolet Imager (SUVI) on board the GOES-16 satellite. These observations provide a good imaging coverage of the event from the low corona to ~30 $R_\odot$ (the outermost field of view of LASCO/C3). LASCO saw the CME above the eastern solar limb (see Figs. 2 and 4). The Coordinated Data Analysis Workshop (CDAW) LASCO CME catalog[2] reported it as a full halo, because eventually the CME-related structures surrounded the occulting disk of the coronagraph.

2.3.1. Extreme ultraviolet wave observations

The EUV wave was observed by both STEREO-A and near-Earth spacecraft (e.g., SDO/AIA and GOES/SUVI). As seen from Earth, the AR12790 was located just behind the eastern limb, and so the EUV wave was observed by AIA to propagate above the eastern limb and also along the solar surface at the eastern hemisphere. From STEREO-A/EUVI, the AR12790 was visible on the solar disk, and so the EUV wave expansion along the solar surface was best observed from this viewpoint.

Figure 2a shows observations before (a1 plain image) and during (a2 running-difference image) the eruption from STEREO-A/EUVI at 195 Å. The EUV wave propagated from the AR12790 along almost all directions (see the online movie 1; the movie is produced by wavelet processed images of STEREO-A/EUVI[3] (Stenborg et al. 2008)). The wavefront was particularly bright from around 12:55 to 13:10 UT, suggesting the formation of a strong compressive wave (probably a shock wave). The EUV wave, which initially propagated coherently along the solar surface for at least 15 min, started to deform after ~13:15 UT, and progressively became dimmer and more diffuse with time, indicating that the wave may have been weakening progressively in the low corona.

The propagation of the EUV wave seemed to be affected (and even interrupted) by the ARs and coronal holes that it encountered during its expansion. Previous studies suggest that the coronal features which an EUV wave encounters could affect its propagation (e.g., Long et al. 2011, 2017; Olmedo et al. 2012; Kwon et al. 2013; Hu et al. 2019). The EUV wave expansion towards the western direction seemed to be interrupted by the active regions AR12785, AR12786, and AR12788

---

[2] `cdaw.gsfc.nasa.gov/CME_list`

[3] Available from `http://sd-www.jhuapl.edu/secchi/`

located westward of the parent AR12790 (Fig. 2a1). After the passage of the EUV wave through this ARs complex, it started to deform and became dimmer. It is possible that the wave weakened quickly after the interaction because of the high Alfvén speed expected around ARs at these low coronal heights. We find it difficult to trace any signatures in the low corona that would indicate a wave extension towards the western limb from Earth's perspective.

2.3.2. Coronal mass ejection and white-light shock wave observations

Figures 2b–d show coronagraphic observations in WL from SOHO/LASCO and STEREO-A/COR2. The CME entered the LASCO-C2 and STEREO-A/COR2 fields of view at 13:25 UT and 13:24 UT, respectively. In association with the CME, a WL shock was seen (see Figs. 2b2 and c2) as an intensity front surrounding the CME. Typically, a WL shock wave is observed as a faint propagating intensity front around a CME, and can also be traced by signatures of the deflected streamers (e.g., Sheeley et al. 2000; Vourlidas et al. 2003; Ontiveros & Vourlidas 2009). The WL shock was significantly broader than its driver, the CME, and so the shock wave almost encircled the occulting disk of the coronagraphs even at the early stages of the eruption. The expansion of the wave along the southwest direction resulted in a small deflection of the streamer that was located above the western limb (as labelled in Figs. 2d1 and d2). The deflection was best observed in LASCO-C2 images. Additionally, the shock wave expansion to the north induced the strong deflection of a streamer that was located above the eastern limb (Figs. 2c1 and d1). A similar situation can be deduced from STEREO-A/COR2 observations. The CME from this viewpoint was observed almost face-on and the WL shock can be clearly traced surrounding the CME (see Fig. 2b2). We also observed a streamer deflection above the western limb in STEREO-A/COR2 images (see the labelled region in Fig. 2b2). The WL shock appeared to be more asymmetric in the STEREO-A images compared to LASCO.

2.4. *In situ observations*

Figure 3 shows the magnetic field magnitude and the field components in the spacecraft-centred radial-tangential-normal (RTN; Hapgood 1992) coordinates as measured by the FIELDS instrument (Bale et al. 2016) on board PSP around the arrival of the interplanetary coronal mass ejection (ICME) associated with the 2020 November 29 CME. The plot also shows an earlier ICME most likely associated with the CME on 2020 November 26. Both ICMEs featured a shock (dashed blue lines), sheath (purple-shaded region), and ejecta (aqua-shaded region). In addition, both ejecta showed signatures of a clear flux-rope structure, that is, smoothly rotating magnetic field direction over a large angle. The first ICME (marked with Shock0, Sheath0, and Ejecta0 in Fig. 3) is clearly weaker in terms of the magnetic field magnitude than the second ICME (marked with Shock1, Sheath1, and Ejecta1). Their peak fields are ~10 nT and ~40 nT, respectively. Particle observations at PSP during this period were analysed by Cohen et al. (2021), Giacalone et al. (2021), Lario et al. (2021), and Mitchell et al. (2021).

The shock associated with the 2020 November 29 event (Shock1) passed by PSP on November 30 at ~18:35 UT. The sheath region after the shock was highly turbulent, with large-amplitude out-of-ecliptic field fluctuations. The leading edge of the ejecta was observed on December 1 at ~02:20 UT, and so the passage of the sheath lasted around seven hours. The shock and sheath associated with the 2020 November 29 solar event were also observed by STEREO-A separated by ~39° in longitude from PSP. However, due to the glancing encounter with the spacecraft, no clear flux-rope structure was identified. The shock arrived at STEREO-A on 2020 December 1 at 07:23 UT (not shown). Thus, the difference between the shock arrival times at PSP and STEREO-A is 5.1 h. In spite of the longitudinal separation between both spacecraft, by assuming that the shock was a planar structure, we obtain a radial propagation speed of ~1200 km s^{1} to move from one spacecraft to the other, consistent with the shock speed from the 3D reconstruction above 20 $R_\odot$ described in the following section. The magnetic field coplanarity method yields quasi-parallel shocks at both PSP and STEREO-A, with the angle between the upstream magnetic field and the shock normal being ~36° and ~31°, respectively. We note that as the magnetic field in the downstream region of the shock exhibited strong fluctuations, these values are given here with rather low confidence. The interplanetary shock waves were strong, the downstream to upstream magnetic field ratios at PSP and STEREO-A being 4.5 and 7.6, respectively. At SolO and Earth, there was no evidence of an interplanetary shock wave passage. This suggests that the interplanetary extent of the shock wave covered at least ~40° in longitude because PSP and STEREO-A observed the interplanetary shock wave (or ~80° assuming symmetry around the source region), and less than ~95° because neither SolO nor Earth observed the shock.

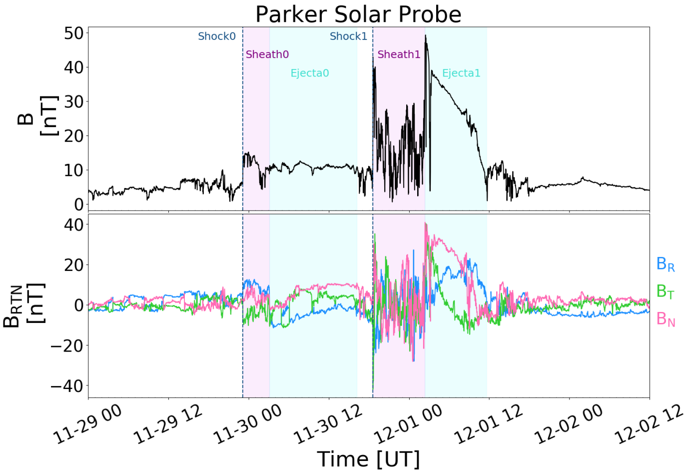

Fig. 3. PSP magnetic field data measured at a distance of 0.81 au during the solar event on 2020 November 29. *Top panel*: magnetic field magnitude and the *bottom panel* the field components in the RTN coordinate system. The interval shows both the ICME associated with the main eruption of interest on 2020 November 29 (Shock1, Sheath1 and Ejecta1) as well as the ICME associated with an earlier eruption on 2020 November 26 (Shock0, Sheath0 and Ejecta0). Shocks are indicated by dashed blue lines. The sheath and ejecta intervals are shaded in purple and aqua, respectively.

2.5. *Shock wave and CME reconstruction*

In order to determine the position and kinematics of the shock in the corona, we reconstructed its 3D structure using the geometrical ellipsoid model developed by Kwon et al. (2014). The model uses seven free parameters for the ellipsoid model, namely the longitude, latitude, and height of the ellipsoid centre, the lengths of the three semi-principal axes, and the rotation angle of the ellipsoid (more details given in Kwon et al. 2014). Observations from different viewpoints are essential to achieving an accurate fit of the geometrical ellipsoid model to the pressure/shock wavefront. We took advantage of the two viewpoints provided by STEREO-A and near-Earth spacecraft (i.e. SOHO and SDO), and applied the geometrical model using EUV and WL observations from these spacecraft. The free parameters were adjusted to achieve the best visual fit of the geometrical ellipsoid model with near-simultaneous observations for all the available viewpoints. We started the reconstructions of the shock or pressure wave at ~12:50 UT by fitting the geometrical ellipsoid model to the EUV wave observations and we continued with the fitting of the WL shock to the coronagraphic observations until 16:00 UT. Figure 4 shows running difference EUV and coronagraphic images from STEREO A-EUVI, COR-1 and COR-2, SDO/AIA, and SOHO/LASCO-C2 and C3. Over plotted in these images is the ellipsoid obtained by the geometrical ellipsoid model of Kwon et al. (2014).

The pressure/shock wave appears on the EUV and WL images as a brightening enhancement around the CME (i.e. see Ontiveros & Vourlidas 2009; Kwon et al. 2013) as a consequence of a density increase produced by the passage of the disturbance driven by the CME. Such a density increase may not constitute a magnetosonic shock but only a compressive pressure wave that has not yet steepened into a shock. In addition, we note that the use of an ideal geometrical shape (e.g., an ellipsoid) to describe the actual large-scale shock structure is a compromise that implies some approximation. The pressure/shock wave surface could have a globally deformed structure as it propagates away from the Sun, which may result in discrepancies to the shape fitting. These deformations tend to be observed mostly at regions where the shock interacts with streamers and coronal holes due to the rapid changes in the local fast magnetosonic speed (e.g., Kwon et al. 2013). The final shock reconstruction is obtained by adjusting the free parameters of the geometrical model until a visually satisfied fit is achieved.

The panels on the right column of Fig. 4 show the position of the ellipsoid as seen from the north ecliptic pole at different times. We also show the nominal Parker spiral field lines connecting each spacecraft (e.g., PSP (black), SolO (yellow), STEREO-A (red), and Earth (green)) with the Sun, considering the solar wind speeds of Table 1. We use grey colour for the downstream part of the field lines once the field lines are found to be connected to the partial ellipsoid model. To determine whether or not the shock connects to each spacecraft field line, we estimated the 3D angular width of the shock using the method presented in Kwon & Vourlidas (2017). As shown in Fig. 4, we include a hole in the ellipsoid model that appears in the lower part of it. The angular width of this hole is determined from the EUV and WL coronagraphic observations so that a good fit to the overall halo envelope at the far flanks of the CME is achieved in all viewpoints. Because there are no signatures of the shock wave beyond the points where the streamers were deflected, this affects the estimation of when the Earth connected with the shock. We find that for PSP, SolO, and STEREO-A a magnetic connection with the shock wave has been established by around 13:30 UT, whereas the time of connection with Earth probably happens much later by around 15:20 UT. At the time when the shock connects to Earth, it propagates into larger coronal heights, and so the estimation of the angular width from the formed halo front and the estimated connection times are more uncertain.

From the shock wave reconstruction, we determined the kinematics of the shock nose and flanks (see Fig. 5). The bottom panel of Fig. 5 shows that the shock is first accelerated to ~1900 km s^{-1} until 13:30 UT, when the shock apex was located at around 6 $R_{\odot}$. Subsequently, the shock decelerated, and near the end of the reconstruction interval at ~16:30 UT, the speed at its apex has fallen to ~1300 km s^{-1}.

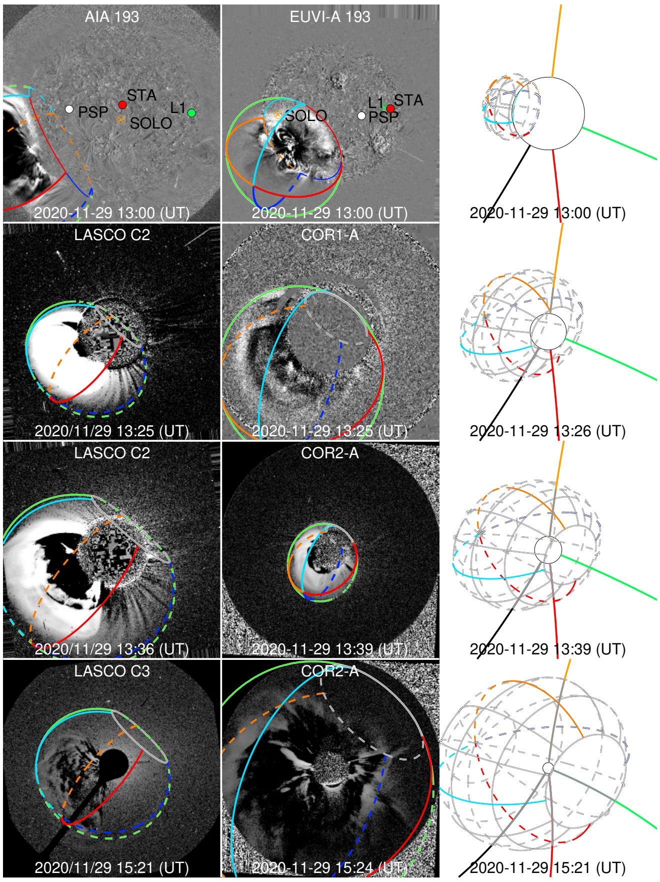

Fig. 4. Three-dimensional shock reconstruction based on the geometrical ellipsoid model of Kwon et al. (2014). *Left and middle column panels*: running difference EUV and WL coronagraphic images of the solar corona, from near-Earth instruments (SDO/AIA at 193 Å and SOHO/LASCO-C2 and C3) on the left, and from STEREO-A (EUVI at 195 Å and STEREO-A/COR1 and COR2) in the middle. The ellipsoid fitted to the shock front is over-plotted. The red, orange, blue, and cyan coloured lines represent the four quadrants of the modelled ellipsoid. The white circles are used to indicate the intersection of the ellipsoid with the solar surface (the dashed lines are used when the structure is on the far side of the Sun from the observer's point of view). On the *top panels*, the coloured symbols mark the footpoints of the nominal Parker spiral field lines that connect to PSP (white), SolO (yellow), STEREO-A (red), and Earth (green). The *right column* shows the position of the ellipsoid projected at the ecliptic plane as seen from the northern ecliptic pole and the nominal Parker spiral field lines that connect to PSP (black), SolO (yellow), STEREO-A (red), and Earth (green).

A 3D reconstruction of the CME (from ~3.5 to ~21 $R_{\odot}$) using the Graduated Cylinder Shell (GCS) model (Thernisien et al. 2006; Thernisien 2011) was performed by Nieves-Chinchilla et al. (2022). The reconstruction of this CME was difficult, as its structure departed from a typical CME. Its southern portion expanded to a greater extent and its leading edge was flatter than the one modelled by the GCS shape. This latter difference was particularly notable in the SOHO/LASCO images (see Fig. 2c2 and d). The resulting CME angular extent in the equatorial plane based on Dumbović et al. (2019) is ~74° and the CME propagation speed at a height of 20–30 $R_{\odot}$ is ~1780 km s^{-1} at the leading edge.

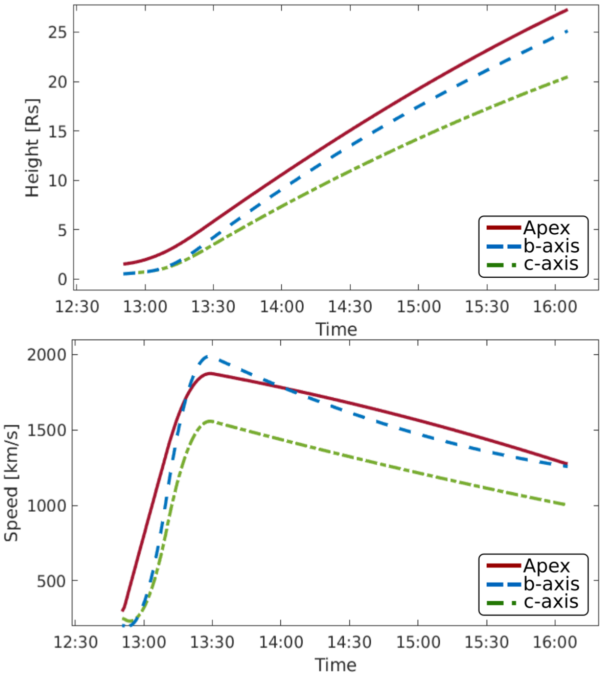

Fig. 5. Height and kinematic time profile of the reconstructed shock wave using the geometrical ellipsoid model. *Top (bottom) panel*: height (speed) of the shock apex measured from the Sun centre and the lengths (speeds) of the two semi-principal axes of the model.

3. Modelling

3.1. Shock modelling in 3D

In this section, we derive the 3D properties of the reconstructed pressure/shock wave using the methods presented in Rouillard et al. (2016), Plotnikov et al. (2017), and Kouloumvakos et al. (2019). We started from the time sequence of the ellipsoids fitted to the observed shock wave and calculated the speed of the shock surface in 3D. From the shock wave speed and the upstream MHD parameters of the background corona, we computed the shock's Mach numbers (Alfvénic (M_A) and fast magnetosonic), compression ratios (e.g., the density compression ratio, X), and the magnetic field obliquity with respect to the shock normal (θ_{BN}). In this study, the ambient plasma density, temperature, and magnetic field of the background corona are provided by the Magneto-hydrodynamic Around a Sphere (MAS) model from the solar surface to $30\,R_\odot$. This model was developed by Predictive Science Inc. (Lionello et al. 2009; Riley et al. 2011).

For the MAS model, we used the radial component of the magnetic field based on SDO/Helioseismic and Magnetic Imager (HMI) synoptic maps as an inner boundary. The parent AR12790 was located behind the east limb during the event; we therefore combined most of the HMI data for CR2237 (Carrington rotation) and some from CR2238. Additionally, we used an improved method for estimating the polar magnetic flux and filling the unobserved portions of the magnetic field for the MAS simulation used in this study. The net flux is estimated as a function of latitude by analysing the zonally averaged HMI data product over time, and modifying the polar filling technique from Mikić et al. (2018), which includes small-scale flux concentrations and parasitic polarities in order to exactly match the estimated net flux in the filled regions. The MAS model also includes detailed thermodynamics with realistic energy equations accounting for thermal conduction parallel to the magnetic field, radiative losses, and parameterized coronal heating. The coronal heating model used here is the wave-turbulence-driven model, which is a 3D version of the 1D formulation studied comprehensively by Downs et al. (2016), and the radiative loss function was determined from CHIANTI 7.1, assuming 'hybrid' abundances.

We used the results of the shock model to calculate the temporal evolution of the shock parameters along the full shock surface. We present these results in Appendix A. Additionally, Fig. 6 shows a snapshot of the modelled wave (top row panels) at 13:19 UT from a view of the ecliptic plane as seen from solar north. The colour maps plotted on the ellipsoid surface show the calculated distributions of the shock parameters. Figures 6a–c show the shock's Alfvénic Mach number, the density compression ratio, and the magnetic field obliquity with respect to the shock normal, respectively. We also show the nominal Parker spiral field lines connecting each spacecraft to the Sun surface as in Fig. 4. From Figs. 6a and b we see that there are multiple regions along the wavefront where a strong shock ($M_A > 3$ and $X > 3$) was formed by 13:19 UT. These regions are located mainly at the north, northeast, and northwest flanks of the wave, as well as at some locations near the apex. Those regions are mostly located close to the neutral line of the heliospheric current sheet where the Alfvén speed is low because the magnetic field is weak and the plasma density is high. The shock strength (e.g., the Mach number) at these regions can be significantly enhanced (Rouillard et al. 2016). Additionally, efficient ion acceleration at the shock wave is expected to take place at these regions (Afanasiev et al. 2018; Kouloumvakos et al. 2019, 2020a). The shock wave at these locations is supercritical and strong, and therefore it is expected that a significant portion of the upstream ions can be injected into the acceleration process.

From Fig. 6c, we see that the shock geometry is mainly quasi-parallel at the shock apex. The magnetic field lines are nearly radial and almost aligned to the shock normal direction near the apex which is located at $\sim 4\,R_\odot$. There are extended regions at the shock flanks where the geometry is mainly quasi-perpendicular. In Fig. 6c, we mark some of these regions located at the northern flank. The WL coronagraphic observations show that the shock wave interacts with a streamer located above the eastern limb (e.g., Fig. 2). This interaction is best observed in LASCO-C2 images at ~13:48 UT, where there is a clear deflection of the streamer (Fig. 2d1). These regions, where the shock geometry is almost perpendicular, could be places of efficient electron acceleration by the shock-drift mechanism (e.g., Mann et al. 2018; Kouloumvakos et al. 2021) if a supercritical shock wave has also formed.

3.2. Magnetic field configurations

3.2.1. Magnetic connectivity in the inner heliosphere

We continued our modelling by estimating the interplanetary magnetic field configuration near the start of the eruption in the inner heliosphere and the magnetic connectivity of the different spacecraft from their locations to 0.1 au. The first and simplest model is to assume a nominal Parker spiral that connects the observers to the corona. The curvature of the Parker spiral and therefore the longitude of the magnetically connected footpoints is controlled by the solar wind speed (which can be taken from the in situ solar wind measurements as in Fig. 1). In this model, the solar wind speed is assumed to remain constant from the observer to the corona. In addition, the impact of previous events cannot be accounted for, and therefore we

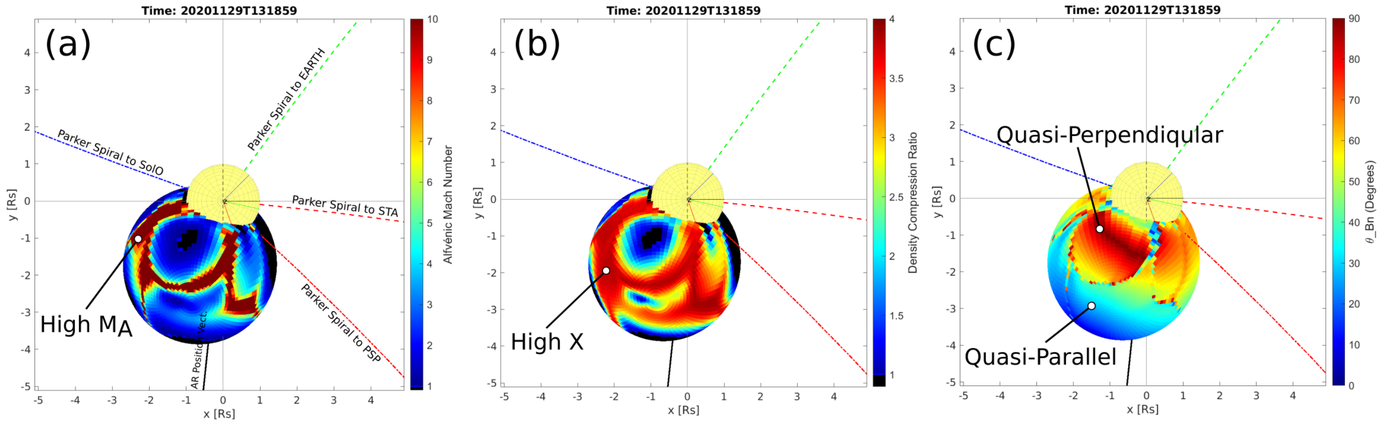

Fig. 6. Selected snapshots of the modelled shock wave parameters in 3D plotted along the reconstructed pressure wavefront surface. The Sun (yellow sphere) is plotted to scale at the centre and the coloured meridians visible on the surface represent the solar central meridian as viewed from STEREO-A (red) and Earth (green). The reconstructed pressure wavefront surface at 13:19 UT is shown and the different shock parameters plotted on the wavefront surface are: the Alfvén Mach number (M_A) in (*a*), the density compression ratio (X) in (*b*), and the angle between the shock normal and the upstream magnetic field (θ_{BN}) in (*c*). The nominal Parker spiral field lines connecting the Sun surface to each spacecraft are plotted on each panel.

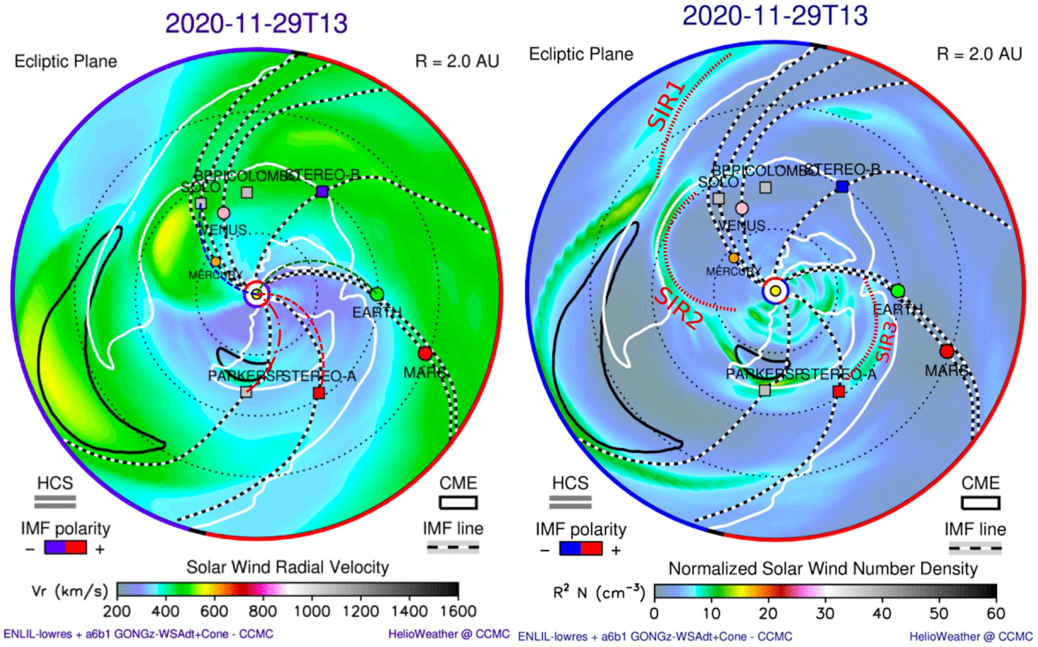

Fig. 7. Plots from the ENLIL simulation in the ecliptic plane near the time of the eruption on November 29. *Left panel*: solar wind radial velocity contours and the *right panel* the normalized solar wind number density. Black and white dashed lines show the simulated magnetic connectivity of the different spacecraft around the particle release time. In the left panel we also show the Parker spirals connecting the spacecraft to the solar surface (see Fig. 1) and in the *right panel* we mark regions where SIRs are likely developed. The traced ICMEs are outlined by a black contour. The white lines represent the HCS, which separates the regions with opposite magnetic polarity, shown in blue (negative) or red (positive) on the outer edge of the simulation region. The Sun in the centre is not to scale.

model the changing solar wind conditions using a 3D MHD model, including previous events that could have an impact on the magnetic connectivity estimates. In this study, we used the Wang-Sheeley-Arge (WSA)-ENLIL+Cone model (ENLIL model, Odstrčil et al. 1996; Arge & Pizzo 2000; Odstrcil 2003), as implemented under the National Aeronautics and Space Administration's (NASA) Community Coordinated Modeling Center (CCMC), to simulate the solar wind conditions before the main eruption on 2020 November 29. In Appendix B, we give further details of the WSA-ENLIL+Cone model setup.

Figure 7 shows a snapshot from the modelling results of the WSA-ENLIL model near the start time of the eruption on 2020 November 29. In this view of the ecliptic plane as seen from the solar north, the colour scale represents the simulated solar wind speed and the black and white dashed lines show IMF lines connecting to different spacecraft and planets. The input parameters and further results of this run are available on the CCMC website[4]. From Fig. 7 we show that previous CMEs (the ICMEs indicated by the black contours in Fig. 7) can have an impact on the magnetic configuration in the inner heliosphere and hence on the magnetic connections of the spacecraft to the Sun, as might

---

[4] `https://ccmc.gsfc.nasa.gov/database_SH/Laura_Rodriguez-Garcia_051121_SH_1.php`

Table 1. Location of the footpoints magnetically connected to the spacecraft from the results of the ENLIL simulation and the nominal Parker spiral.

(1) s/c	ENLIL (2) Lon. [(a)]	(3) Lat. [(a)]	(4) ΔLon. [(b)]	Parker spiral (5) V_{sw}	(6) Lon. [(a)]	(7) Lat. [(a)]	(8) ΔLon. [(b)]
PSP	294°	4°	45°	295 [(c)]	319°	4°	69°
STA	340°	7°	91°	361	355°	7°	106°
SolO	142°	−5°	−107°	417 [(c)]	162°	−5°	−88°
Earth	37°	0°	148°	358	55°	1°	166°

Notes. [(a)]The longitude and latitude values are given in the heliographic Carrington coordinate (HGC) system. The locations of the footpoints from the ENLIL simulation are given at 21.5 $R_\odot$, which is the inner boundary of the simulation, and for the nominal Parker spiral are given at the solar surface. [(b)]The longitudinal separation angle is calculated from the flare location at 249° longitude (in HGC). [(c)]Solar wind values from ENLIL simulation used on 2020 November 29 at 13:00 UT.

be the case for PSP. Based on Fig. 7, it seems that the outward propagation of the preceding CMEs has modified the spiral orientation for PSP in what appears to be a slight rarefaction region. Additionally, interplanetary structures such as stream interaction regions (SIRs), which are formed by the interaction of a faster solar wind stream with the preceding slower solar wind, can also affect the connection of the different spacecraft during the event. This seems to be the case for SolO, where on November 30 an enhanced magnetic field structure is observed and is most likely a SIR as discussed in Kollhoff et al. (2021). In the right panel of Fig. 7, we mark the locations where possible SIRs have been formed. SIR1 and SIR2 were possibly observed in situ by SolO on November 27 and 30, respectively (see Fig. 2 in Kollhoff et al. 2021). SIR3 was observed in situ on November 30 by near-Earth instruments and at around the same date enhanced density structures were observed in situ by STEREO-A. In Appendix B, we show a comparison between the results of the ENLIL simulation and in situ solar wind measurements.

From the ENLIL simulation, we derived the locations of the footpoints of the magnetic field lines connecting to each spacecraft by tracing the field lines from the different spacecraft locations towards the inner boundary of the model at 21.5 $R_\odot$. In Table 1 we list the location of the footpoints of the field lines connecting to each spacecraft obtained from the results of the ENLIL simulation (Cols. 2–3) and obtained by assuming the nominal Parker spiral field lines (Cols. 6–7), whereas ΔLon. provides the longitudinal separation between the flare site and the footpoints of each spacecraft (Cols. 4 and 8 estimated using the ENLIL and the Parker method, respectively). As displayed in Fig. 7, there is a tendency for the ENLIL simulation to locate the magnetic footpoints towards more eastern longitudes than the footpoints obtained assuming a Parker spiral. A possible reason for this is the changes of the solar wind speed due to intervening structures, such as prior CMEs and SIRs (Fig. 7), which the Parker model cannot account for. The largest differences between the two connectivity estimates is found for PSP where we find that the footpoints from the ENLIL simulation that are magnetically connected to the spacecraft are shifted towards eastern longitudes and located ~24° closer to the flare location. For the other probes, this difference is smaller (see Table 1).

3.2.2. Magnetic connectivity in the low corona

As the next step in this analysis, we examined the magnetic field configurations and magnetic connectivity in the low corona using two different connectivity models. In the first model, we used the magnetic field vector data from the MAS 3D cubes and performed a field line tracing to estimate the magnetic field configurations. We estimated the magnetic connectivity of the different spacecraft, focusing on the regions around the IMF lines connecting to the spacecraft. For the IMF lines, we used the results of the analysis presented in the previous section from the two models. These are the nominal Parker spiral and the ENLIL model. We started the field line tracing (FLT) around these regions and at a height of 3.0 $R_\odot$, continuing the computation sunward (antisunward) until the tracing reached the inner (outer) boundary of the MAS simulation domain (1 to 30 $R_\odot$). We considered every open-field line located inside an angular distance of 10° from the location of the footpoints of the connected IMF lines. This angular distance can be considered as a typical uncertainty of the magnetic connectivity estimates. We expect that the magnetic field lines meander in space at a characteristic angular scale of 10° (e.g., Nolte & Roelof 1973). This is similar to the typical size of solar supergranules (Giacalone & Jokipii 2004). Therefore, following the process described above, we arrived at two different magnetic connectivity estimates, one considering the Parker spirals and the MAS field lines (PS+MAS) and the other the ENLIL IMF and the MAS field lines (ENLIL+MAS).

Figure 8 shows the magnetic configurations in the low corona and the connectivity results using the magnetic field vector data from the MAS 3D MHD data cubes. Figure 8a shows the result of the full field line tracing (open and closed field lines) in 3D, and 8b and 8c show the open field lines connecting to the different spacecraft and locations (e.g., STEREO-A, PSP, and Earth) from the ENLIL+MAS or PS+MAS connectivity estimates, respectively. For PSP and STEREO-A we find that the magnetic connectivity at the solar surface is similar in both cases but the field lines seem to diverge significantly above the solar surface towards different longitudes. PSP is connected to field lines located near the eastern side of the AR12785-6 complex (see Figs. 8b and c), whereas STEREO-A is connected to the field lines located near the centre of the same AR complex. Specifically, we find that the footpoints of the connected field lines to PSP are located at a Carrington longitude (CRLN) of ~326° and ~329° from ENLIL+MAS and PS+MAS connectivity estimates, respectively, and the connected field lines to STEREO-A at CRLN ~349° and ~352°. The magnetic connectivity of Earth is significantly different in the ENLIL+MAS and PS+MAS connectivity estimates. From PS+MAS, we find that the footpoints of the connected field lines to Earth are located at CRLN ~58°, while from the ENLIL+MAS we find that the

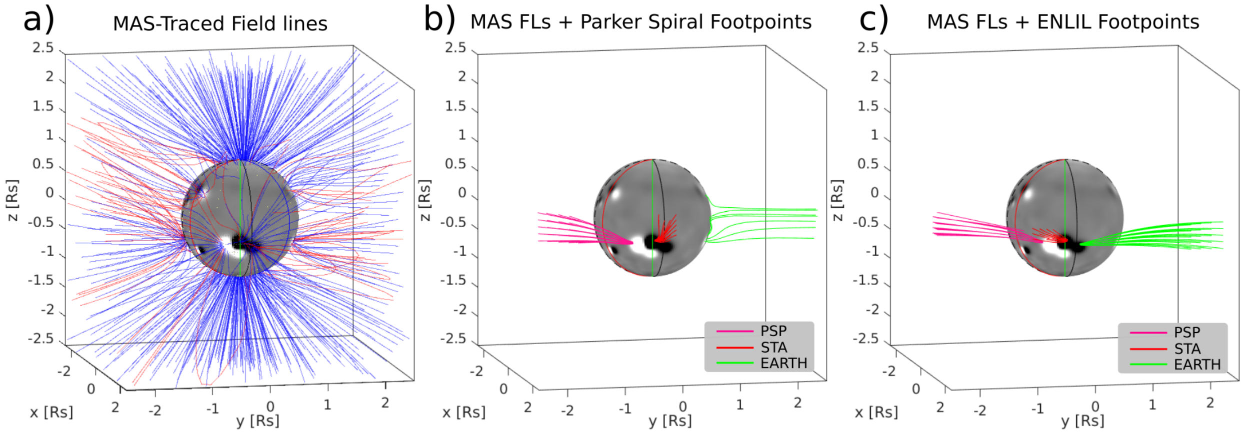

Fig. 8. Magnetic configurations in the low corona and the connectivity results using the magnetic field vector data from MAS 3D MHD data cubes. *Panel a*: magnetic field configurations in the low corona from the MAS MHD model. Plotted are open (blue) and closed (red) field lines traced using the magnetic field vector data from the MAS 3D cubes. *Panels b, c*: field lines of magnetic connectivity between the Sun and the spacecraft estimated from the traced field lines and the location of the footpoints of the connected IMF lines from the nominal Parker spiral (*panel b*) or the ENLIL model (*panel c*). The Sun is represented to scale by the radial magnetic field at the solar surface from the MAS data.

footpoints are located near the western side of the AR12785-6 complex at CRLN ∼4°.

To give further context to our magnetic connectivity estimates, we also used the Institut de Recherche en Astrophysique et Planétologie (IRAP) 'connectivity tool'[5] (Rouillard et al. 2020). First, we calculated the magnetic field configurations using the Potential Field Source Surface (PFSS) model (Schatten et al. 1969; Schrijver & De Rosa 2003) and then we estimated the magnetic connections of the different spacecraft to the solar surface. The connectivity tool performs simultaneous estimates of connectivity based on different combinations of models and boundary conditions rather than relying on a single model or data set. The tool considers a Parker spiral from an observer to the outer boundary of the coronal model and from this point it estimates the magnetic connectivity in the low corona. For every spacecraft, the tool provides the connectivity solutions for a measured value of the solar wind speed if it is available, or two solutions, one for slow ($300\,\mathrm{km\,s^{-1}}$) and one for fast ($800\,\mathrm{km\,s^{-1}}$) solar wind if in situ measurements are not available.

In this study, we used the PFSS model and global photospheric magnetic maps. The PFSS model takes global maps of the radial magnetic field at the photosphere and produces the magnetic field in 3D from the solar surface to the height of the source surface (at $2.5\,R_\odot$). For the input magnetic maps, we used the maps provided by the Air Force Data Assimilative Photospheric Flux Transport (ADAPT) model (Arge et al. 2010, 2013). The ADAPT maps are global magnetograms of the photospheric magnetic flux. They are produced using data assimilation techniques along with a magnetic flux transport model (Worden & Harvey 2000) and provide different realisations of the photospheric magnetic field at a certain time. Comparing the magnetic configurations produced by the PFSS model of the different ADAPT realisations, we find small differences between the products for this event. Additionally, the modelled magnetic configurations seems to compare well with WL observations, and so we selected the realisation with the best visual comparison (e.g., Poirier et al. 2021). To estimate which field lines connect to the spacecraft, we followed the same procedure as that presented for the MAST model (Lionello et al. 2009; Riley et al. 2011), using the location of the IMF lines from both the nominal Parker spirals and the ENLIL model.

Figure 9 shows the magnetic configurations in the low corona using the PFSS model (left panel) and the results from the connectivity analysis (middle and right panels), where we show the field lines magnetically connected to PSP, STEREO-A, and Earth overlaid on an EUV image from SUVI at 195 Å before the solar event. The middle panel shows the connectivity results considering the location of the footpoints of the IMF lines from the nominal Parker spiral model. The open magnetic field lines located inside an angular distance of ten degrees from the footpoints location are shown. We also see that PSP is connected to the eastern side of the AR12785-6 complex, STEREO-A is connected to the western side of the AR12785-6 complex, and Earth is connected to a region near the west limb. These estimates are similar to the ones derived from the field lines traced from the MAS 3D cubes. Using the location of the IMF lines from the ENLIL model (see right panel), we find that the magnetic connectivity for PSP and STEREO-A changes towards the eastern helio-longitudes. The magnetic connectivity of Earth is shifted towards the western side of the AR12785-6 complex. This analysis gave us similar results to those we obtained from the connectivity analysis using the MAS data.

4. Evolution of the shock parameters at the field lines magnetically connected to the spacecraft

We examined the temporal evolution of the different shock parameters at the field lines connected to the spacecraft using the magnetic connectivity estimates presented in the previous section, PS+MAS and ENLIL+MAS. We registered the shock parameters at the connecting-to-observer-point (cobpoint) of the connected field lines to each spacecraft and calculated the time history of the distribution characteristics (mean, median, and first and third quartile and first and ninth decile values) of the resulting parameters as a function of time.

Figure 10 shows the temporal evolution of the Alfvénic Mach number (M_A), the density compression ratio (X), and θ_BN at the field lines magnetically connected to each spacecraft. Top (bottom) panels used the PS+MAS (ENLIL+MAS) connectivity estimates. Based on panel a1, which shows the time evolution of M_A using the PS+MAS connectivity estimates, the

---

[5] `http://connect-tool.irap.omp.eu/`

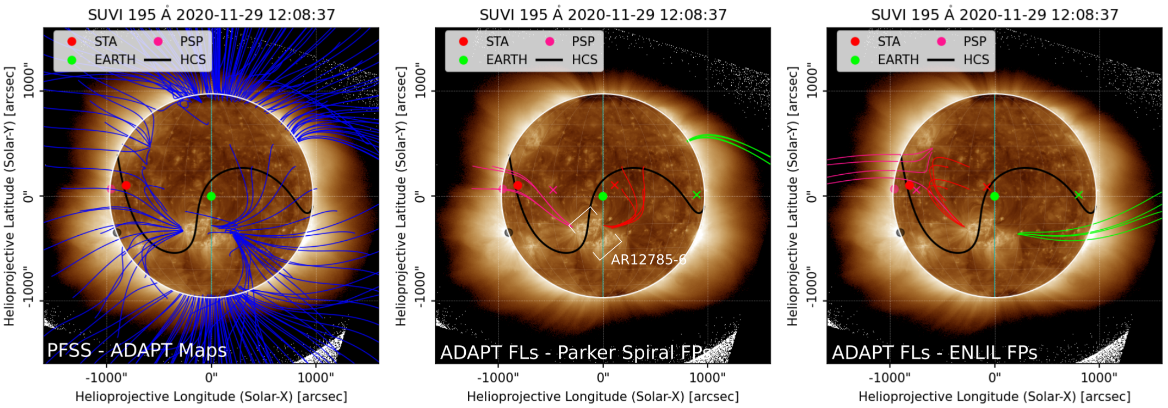

Fig. 9. Magnetic field configurations and connectivity estimates in the low corona using the PFSS model. *Left panel*: magnetic field configurations in the low corona from the PFSS model overlaid on an EUV image of the solar corona from SDO/AIA (only open field lines, in blue, are shown). *Middle and right panels*: field lines of magnetic connectivity between the Sun and the spacecraft. These lines are estimated from the PFSS FLs and the location of the footpoints of the Parker spiral (*middle panel*) or the ENLIL model (*right panel*) IMF lines. The heliospheric current sheet (black line), the location of the spacecraft (coloured circles), and their magnetic connections at the source surface (coloured crosses) projected on the solar surface are shown in each panel.

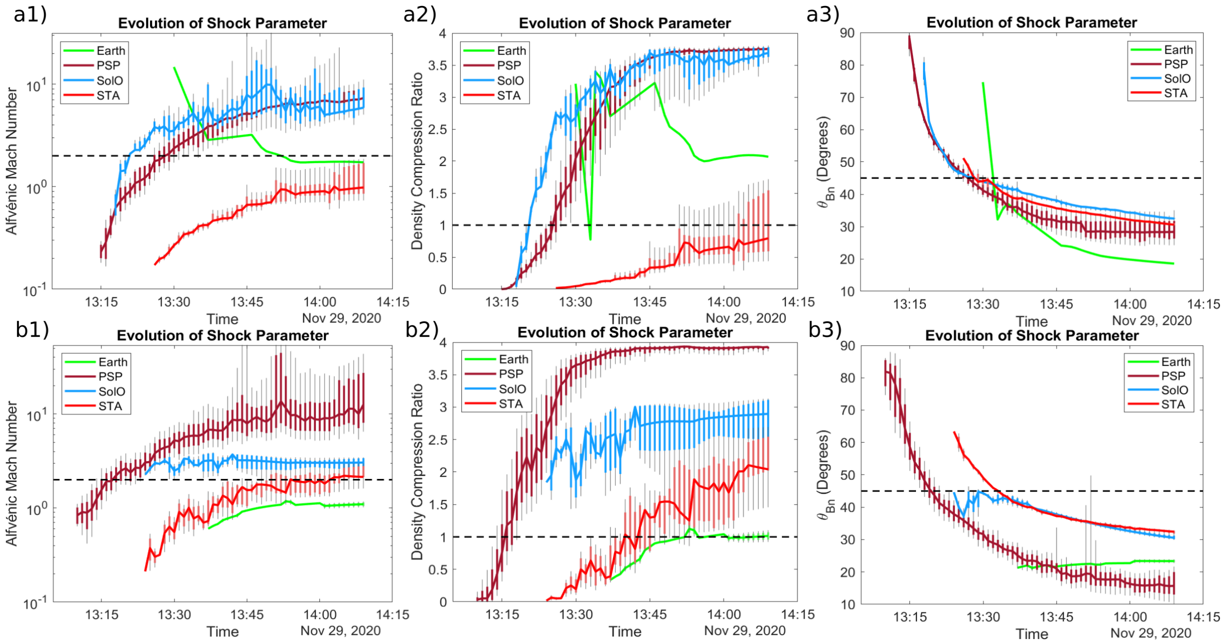

Fig. 10. Temporal evolution of the shock parameters (M_{A}, X, and θ_{BN}) at the field lines magnetically connected to the spacecraft: *panels a1–a3* (*top row*) and *b1–b3* (*bottom row*) respectively show the evolution of the shock parameters for the connected field lines from PS+MAS and ENLIL+MAS. The time-varying distribution characteristics of the shock parameters are presented in each panel. The median values are depicted with the solid lines and the first and third quartile and first and ninth decile are respectively indicated with the coloured and grey vertical bars. The horizontal dashed lines in each panel show: the supercritical limit ($M_c > 2$) in *panels a1 and b1*, the limit of shock formation ($X > 1$) in *panels a2 and b2*, and the oblique θ_{BN} in *panels a3 and b3*.

pressure wave connects to the field lines connecting to PSP for the first time at ∼13:15 UT. A few minutes later, at ∼13:18 UT, the pressure wave connects for the first time to SolO and later on, at ∼13:26 UT, it connects to STEREO-A. However, when the pressure wave magnetically connects to PSP, STEREO-A, and SolO for the first time it has not yet steepened into a shock wave ($X < 1$). We also find that the wave connects for the first time to Earth at ∼13:30 UT which is much earlier than the time presented in Sect 2.5. This happens because we have not limited the angular width of the ellipsoid model when modelling the shock wave because we aimed to examine the evolution of the shock parameters during the earliest possible connection time to Earth. However, for this reason, and because the magnetically connected regions to Earth are located almost diametrically opposite from the eruption site, meaning that the shock model can be highly uncertain in these regions, we interpret the results for the resultant connection times and the shock parameters at Earth with caution.

After the initial connection of the pressure wave with PSP, STEREO-A, and SolO, the strength of the pressure wave (represented by M_{A} and X) continuously increases at the cobpoints of these spacecraft. This can be seen in Fig. 10a2, which shows the evolution of the density compression ratio as a function of time. The pressure wave regions connected to PSP steepen into a shock ($X > 1$) for the first time at ∼13:26 UT. For SolO, this seems to be some minutes earlier at ∼13:21 UT, while for STEREO-A this happens much later at ∼14:03 UT (we used the third quartile values here). Overall, we find that SolO (PSP) connects to strong shock regions 1 to 3 min (8 to 14 min) after the time that the pressure wave magnetically connects to the spacecraft. For these spacecraft, the M_A first and third quartile values range between ∼4 and ∼9 when the shock strength reaches a plateau (after 13:45 UT). The density compression ratio first and third quartile values range between 3.1 and 3.8 after 13:45 UT. For STEREO-A, we find that the connected shock regions are very weak. The M_A and X pass above one only for some regions near the end of the modelling interval. During the early stages of the magnetic connections, the shock geometry is mainly quasi-perpendicular ($\theta_{Bn} > 45°$) for PSP and SolO. The geometry changes progressively from quasi-perpendicular to oblique ($\theta_{Bn} \sim 45°$) and then progressively changes from oblique to quasi-parallel ($\theta_{Bn} < 45°$). We find that for both PSP and SolO the shock takes 15 min to evolve from a quasi-perpendicular to an oblique geometry, and 30 min from oblique to quasi-parallel geometry. For STEREO-A, at first connection θ_{Bn} was close to oblique and then it gradually evolved to quasi-parallel.

Figures 10b1–b3 show the temporal evolution of the shock parameters at the field lines magnetically connected to each spacecraft using the ENLIL+MAS connectivity estimates. In Sect. 3.2.1 we show that the magnetic connectivity of PSP, STEREO-A, and Earth shifts towards the eastern heliolongitudes low in the corona when considering the IMF lines from the ENLIL model. As the PS+MAS and ENLIL+MAS approaches give different connectivity estimates, we expect the resultant temporal evolution of the shock parameters to differ also. This is evident by comparing the top-row (PS+MAS) and bottom-row (ENLIL+MAS) panels (the y-axis scale is the same to enable a direct comparison) of Fig. 10. Some clear differences can be seen in the temporal evolution of the shock strength (M_A and X) which are on average higher (lower) for PSP and STEREO-A (SolO) in the ENLIL+MAS case than for PS+MAS. This is related to the fact that between the PS+MAS and ENLIL+MAS magnetic connectivity estimates, the locations of the connected field lines respectively change from the shock flanks towards the shock apex for PSP and STEREO-A, but from the shock apex towards the flanks for SolO.

There are also some differences in the first connection time to the different spacecraft for the ENLIL+MAS case. Specifically, as can be seen in the bottom-row panels of Fig. 10, we find that shock wave regions are almost immediately connected to SolO at ∼13:25 UT. When the pressure wave reaches the field lines magnetically connected to SolO it has already steepened into a shock wave. Additionally, the first shock regions ($X > 1$) connect to PSP at ∼13:16 UT and to STEREO-A at ∼13:40 UT. In the case of Earth, we find that the connection to a shock region is significantly delayed, as this happens at ∼13:53 UT. As noted earlier we have not limited the angular width of the ellipsoid model when determining the connection time to Earth. At PSP we estimate that after 13:40 UT (when the shock strength reaches a plateau) the M_A first and third quartile values[6] range from ∼6 to ∼14 and X range from ∼3.8 to ∼3.9. Therefore, PSP is magnetically connected to strong shock regions for a long time. SolO is connected to weaker shock regions compared to PSP. However, these regions are supercritical ($M_A > 2.0$)[7], with M_A first and third quartile values ranging from 2.3 to 3.7, and X ranging between 2.3 and 3.0. We find that the shock regions connected to STEREO-A are weaker than those connected to SolO. The shock strength is overall higher than the values presented in Fig. 10a1, with first and third quartile M_A values ranging between 1.1 and 2.8 after 13:44 UT and median M_A values passing just above the supercritical limit after 13:54 UT. In the same time interval, X increases from unity to around two. Finally, we note that Earth is magnetically connected to weak shock wave regions long after the first connection takes place. The density compression ratio value is close to one during the shock modelling interval.

We compared the temporal evolution of the shock parameters at the field lines magnetically connected to each spacecraft with the inferred release time of the SEPs observed by each spacecraft. For the SEP release times, we used the values presented in Kollhoff et al. (2021). In that study, the SEP release times were determined by performing velocity dispersion analysis (VDA) and time-shifting analysis (TSA) determined for each spacecraft (e.g., Vainio et al. 2013). Table 2 summarises the results of the estimated SEP release times with their uncertainty (the light travel time has been added to these times to compare them with the electromagnetic observations). At three of four spacecraft (SolO, STEREO-A, SOHO) the inferred release times suggest that the release of energetic electrons occurs before the release of energetic protons.

To enable a comparison between the SEP release times and the evolution of the shock parameters at the field lines magnetically connected to each spacecraft, we defined three characteristic times: (1) when the pressure wave connects to the spacecraft, (2) when the connected regions steepen into a shock wave, and (3) when the connected shock regions become supercritical on average. We determined characteristic times for both the PS+MAS and ENLIL+MAS magnetic connectivity estimates and list them in Table 2.

Figure 11 (similar to Fig. 9 in Kollhoff et al. 2021) shows a timeline of the solar events that occurred before and during the SEP event. The vertical bars show the angular distance of the spacecraft magnetic field footpoints from the flare location using the connectivity estimates from (a) PS+MAS and (b) ENLIL+MAS. The release times were estimated using the VDA or the TSA (shown with subscripts ‘V’ and ‘T’, respectively). In this figure, we also show the three characteristic times for the evolution of the shock parameters that we defined earlier. We compared them with the solar release times of electrons and ions observed by the different spacecraft. First, we find that the electron and proton release times for each spacecraft are later than the first time when the pressure wave magnetically connects to the spacecraft in all cases. Therefore, the propagation or expansion of the pressure wave to distant heliolongitudes is probably responsible for the observed particle release at each spacecraft. We find that the energetic electron release times are close to the times where the pressure wave steepens into a shock and/or when the connected shock becomes supercritical for most of the cases. On the other hand, we find that the energetic proton release times are delayed from the shock characteristic times.

According to Kollhoff et al. (2021), the release time of energetic protons observed by PSP occurred at 13:23 UT, whereas the energetic electrons occurred at 13:27 UT with an uncertainty of ±5 min. For the PS-MAS connectivity estimate, these release times occur around the time when the connected shock becomes supercritical (from ∼13:25 to 13:28 UT), while for the ENLIL-

---

[6] Without considering some extreme limits appearing in the quartiles.

[7] The critical M_A depends on θ_{Bn} and plasma-beta, and because a shock wave becomes supercritical in the case of an oblique shock geometry and under coronal conditions at M_A of ∼2, we use this value throughout our study.

Table 2. Timeline of the 2020 November 29 SEP event.

s/c	SEP release		Connection times $^{(b)}$ [UT]						M_A	
	Time $^{(a)}$ [UT]		PS+MAS			ENLIL+MAS			PS+MAS	ENLIL+MAS
	Electrons	Protons	First	Shock	Super	First	Shock	Super	Max $^{(c)}$	Max $^{(c)}$
PSP	13:27±05 (T)	13:23(V)	13:15	$13{:}26^{+02}_{-01}$	$13{:}29^{+04}_{-03}$	13:10	$13{:}16^{+03}_{-02}$	$13{:}18^{+05}_{-04}$	7.0	9.7
SolO	13:25±11(T)	14:01±05(T)	13:18	$13{:}21^{+01}_{-01}$	$13{:}21^{+01}_{-01}$	13:24	$13{:}25^{+01}_{-01}$	$13{:}25^{+01}_{-01}$	9.9	3.2
STA	13:30±04(V)	14:55±10(T)	13:26	$^{(\dagger)}14{:}03^{+06}_{-13}$	$^{(\ddagger)}14{:}05^{+4}_{-14}$	13:24	$13{:}40^{+14}_{-03}$	$13{:}54^{+15}_{-06}$	0.9	2.2
Earth	15:32±19(T)	19:02±05(T)	13:30	$13{:}30^{(?)}$	$13{:}30^{(?)}$	13:36	$13{:}53^{+01}_{-01}$	–	3.2	1.1

Notes. $^{(a)}$The respective light travel time has been added to the solar release times in Table 2 of Kollhoff et al. (2021) and the uncertainty in the estimated SEP release times is given in minutes. In the parenthesis, we note the method used for the release time determination, (T) and (V) for TSA and VDA methods, respectively. The energy range used in each case can be found in Table 2 of Kollhoff et al. (2021). $^{(b)}$Characteristic times when the pressure/shock wave connects to the spacecraft. 'First' is the first time when the pressure wave connects to the s/c, 'Shock' is the time when the first shock regions connect to the spacecraft, 'Super' is the time when the connected shock regions become supercritical. For the 'Shock' case the characteristic times are determined when the median values of X become greater than unity and for the 'Super' case when the median values of M_A become greater than the $M_c = 2.0$. The ± values that are given on the right are minutes from the characteristic times that have been determined at the time when the distribution max (min) values pass above the defined thresholds. For $^{(\dagger)}$ we determined the shock connection time from the third quartile values instead of the median. For $^{(\ddagger)}$ we used the third quartile values and $M_c = 1.5$. $^{(c)}$Maximum/plateau values of M_A at the field lines magnetically connected to the spacecraft estimated from the results of Fig. 10. $^{(?)}$Highly uncertain value.

MAS the release times occur between 7 and 11 min after the shock becomes supercritical (see Table 2 and Fig. 11). For SolO, the energetic electrons are released four minutes after the supercritical shock has formed, or simultaneously, depending on the connectivity model. The energetic proton release times at SolO are significantly delayed compared to the onset of the supercritical shock (around 40 min for both models). For STEREO-A, the release of energetic electrons occurs near the time interval where the first shock regions connect to the spacecraft for both connectivity models. For the PS-MAS model, only a few shock regions are supercritical after the electron release, whereas for ENLIL-MAS the shock becomes supercritical, on average, almost half an hour after the electron release. The release of energetic protons at STEREO-A is delayed about one hour compared to the onset of the supercritical shock at ~14:00 UT. For Earth, we find that the formation of a supercritical shock wave is unlikely and the SEP release times for protons and electrons occur many hours after the connection of some weak shock regions to the spacecraft.

5. Discussion

The SEP event on 2020 November 29 was the first widespread event of solar cycle 25 and was observed from four widely separated locations in the inner heliosphere. The event was associated with a solar eruption just behind the east limb as observed from Earth that included an M4.4 class X-ray flare, an EUV wave, and a CME-driven shock. SEP observations show that during the event, energetic particles spread over more than 230° in longitude at spacecraft located close to 1 au. Additionally, the observation of large-particle anisotropies at the onset of the SEP event (Kollhoff et al. 2021; Cohen et al. 2021) suggests that the SEPs were injected over a wide longitudinal range close to the Sun rather than further out due to interplanetary transport processes. However, the expansion of the EUV wave towards the footpoints of these spacecraft is difficult to reconcile with the estimated solar release times of the particles detected at poorly connected spacecraft (see Kollhoff et al. 2021).

In this study, we combined multi-viewpoint remote-sensing observations in order to carry out a detailed examination of the evolution of the EUV wave in the low corona along different directions from the flare location and the evolution of the WL shock wave higher in the corona. We also used these observations to reconstruct the pressure/shock wave and determine its position and kinematics in 3D using a geometrical ellipsoid model and thus infer the shock wave properties and parameters. We estimated the magnetic connectivities between the pressure/shock wave and the different spacecraft using various methods and estimated the time at which the shock wave established magnetic connection with the spacecraft. From the 3D shock model and the connectivity estimates, we examined the temporal evolution of the shock parameters at the connected field lines.

From the EUV observations, we find that the EUV wave initially expanded coherently along the solar surface but later was significantly deformed and weakened. The propagation of the EUV wave was influenced and even interrupted by a complex of ARs located on the southwest side of the parent AR12790, as viewed from STEREO-A. We find that the longitudinal extension of the EUV wave was at least 90° from the flare location for some directions, but that the EUV wave did not reach more distant locations in the low corona. The EUV wave became diffuse and probably weakened before the release of the SEPs at STEREO-A and SolO. This aspect has also been observed and discussed in previous studies for other SEP events (e.g., Lario et al. 2014, 2016; Zhu et al. 2018), where the EUV waves – during their expansion towards the footpoints of the magnetic field lines connecting to spacecraft – became diffuse and untraceable before the SEP release at these locations. The EUV waves being weakened before the release of the SEPs might jeopardise their role in the release and acceleration of particles.

From the 3D shock modelling of the 2020 November 29 event, we find similar characteristics. When the pressure wave reaches the complex of ARs at low coronal heights, its strength reduces significantly because it propagates in a region where the Alfvén speed near the AR is high (Mann et al. 2003; Warmuth & Mann 2005). In this case, the shock wave might be too weak to contribute to the particle acceleration and release at these low coronal locations and this time. However, even if the shock wave is weak in the low corona, this does not exclude the possibility that the shock is stronger at higher altitudes. In this case, the shock wave can contribute to the release of SEPs as

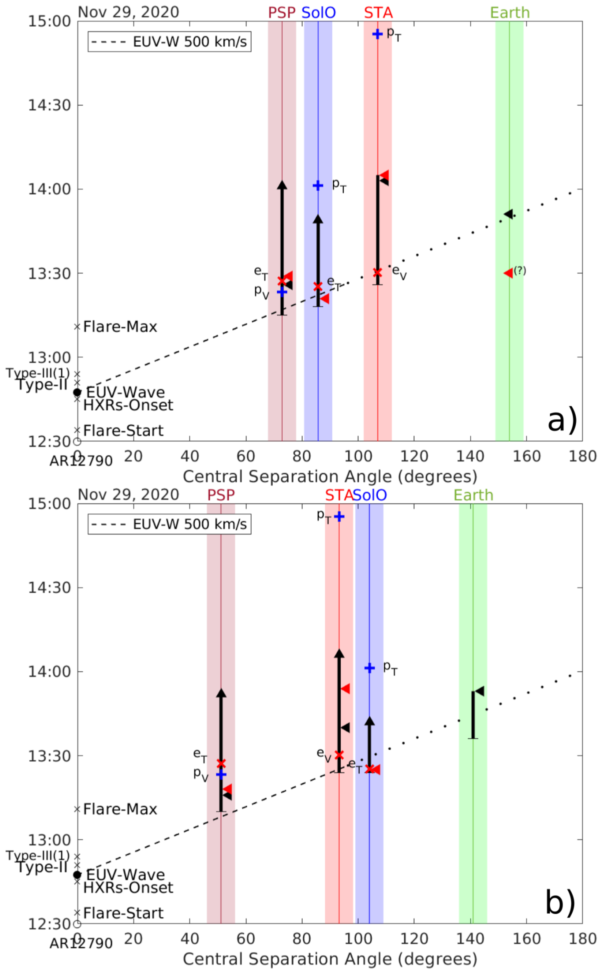

Fig. 11. Comparison of the SEP release times with the characteristic times of the shock wave evolution at the field lines connecting to the spacecraft. For each spacecraft, the angular distance of the magnetic footpoint from the flare location is shown by the vertical bars, which assume an uncertainty of ±5 deg. The time interval when the pressure wave connects to the spacecraft for the first time and the other shock-related characteristic times are shown with the vertical black bar. The time when the shock strength is maximum or reaches a plateau is shown with the black arrowheads at the end of the bar. The time when the connected regions steepen into a shock wave and when the connected shock regions become supercritical on average are shown with the black and red arrowheads beside the bars, respectively. For each spacecraft, the energetic electron and proton release times are shown with red crosses and blue plus symbols and the label subscripts note the method used for the release time determination (see Table 2 for details). For (*a*) we used the connectivity estimates from the PS+MAS and for (*b*) we used those from ENLIL+MAS. The dashed (dotted) line shows the angular distance of the EUV wave from the flare location for an average propagation speed of 500 km s^{-1}.

it expands upwards in the high corona (e.g., Lario et al. 2014; Zhu et al. 2018; Rodríguez-García et al. 2021).

From the coronagraphic observations, we find that the WL pressure/shock wave is significantly broader than the CME and the EUV wave. The 3D reconstruction also shows that the pressure/shock wave expands rapidly in the lateral direction and quickly reaches distant locations in the middle and high corona faster than in the low corona and close to the solar surface. The pressure/shock wave seems to almost encircle the occulting disk of the coronagraphs. This fact is best observed in the WL coronagraphic observations from LASCO-C2, where a clear deflection of the streamer located above the western limb, almost diametrically opposite to the flare, was observed at 13:48 UT. This deflection indicates that the pressure wave rapidly reaches regions located at almost 180° from the flare and higher in the corona, because the deflection of the streamer is observed at around 2.7 $R_{\odot}$.

There are multiple regions where a strong shock ($M_A > 3$ and $X > 3$) was formed early during the eruption based on the 3D shock modelling. Between 12:54 and 12:57 UT, a type II radio burst was observed at 81–45 MHz (Fig. 4 in Kollhoff et al. 2021) confirming that strong shock regions had already formed. At the same time that the strong shock regions formed, we find that the shock geometry evolved from oblique and rapidly changing to quasi-perpendicular in a few minutes until 12:58 UT. This could be an important aspect of the efficient electron acceleration at this time by the shock-drift mechanism and also the production of the type II radio emission, because quasi-perpendicular supercritical shock regions seem to be a key ingredient (e.g., see Zucca et al. 2018; Kouloumvakos et al. 2021). From ~13:00 UT and until the end of the shock modelling interval, the shock's density compression ratio increased and reached a plateau at ~3.2 and the shock geometry progressively changed from quasi-perpendicular to quasi-parallel. We also show that supercritical shock regions form at very distant locations, confirming previous studies. For instance, Kwon & Vourlidas (2018) analysed two events, 2011 March 7 and 2014 February 25, which are associated with SEPs and showed that the angular width of the supercritical region can be much larger than 100° in the low solar corona.

Next, we examined the magnetic field configurations in the corona and IP space and estimated the magnetic connectivity of the spacecraft using different techniques. First, we used the WSA-ENLIL+Cone model to simulate the solar wind conditions before the main eruption. After including previous events, we estimated the magnetic connectivity of the different spacecraft and compared it with the connectivity of the nominal Parker spiral model. We find that the connectivity changes significantly for some of the spacecraft, namely PSP, in which the connection shifts by more than 20° to the east. As we discuss above, the magnetic connectivity of the different spacecraft can be affected by intervening solar wind structures such as SIRs (as is clear from in situ observations in Kollhoff et al. 2021) and previous CMEs included in the simulations. The connectivity estimates of the different spacecraft using the MAS field-line-tracing method or the PFSS model gave similar results. The greatest impact on the final connectivity estimates in the low corona comes from the changes at the location of the footpoints between the ENLIL and the Parker spiral model. We find it difficult to conclude which of the connectivity estimates is the most realistic. However, when we consider the temporal evolution of the shock parameters at the connected field lines and the SEP properties, the connectivity estimates from the ENLIL+MAS model seem more consistent with observations than the PS+MAS. For example, the maximum M_A values are observed at PSP-connected field lines, moderate values are found on SolO and STEREO-A connecting lines, and Earth-connected lines are associated with weak shock strength regions (Table 2). This seems broadly consistent with the apparent ordering of the maximum SEP intensities observed from the different instruments during the SEP event.

From the temporal evolution of the shock parameters at the field lines connected to the different spacecraft, namely PSP, SolO, and STEREO-A, we examined the role of the shock wave in the release of SEPs. For PSP, the shock model suggests that strong shock regions (and supercritical) are quickly connected to the field lines and at the inferred particle release time the shock geometry is mainly quasi-parallel. In addition, the energetic protons are released almost simultaneously with the energetic electrons (within just a few minutes) and both release times are delayed compared to the time at which the wave connects to the field lines for the first time (from 8 to 17 min). The temporal evolution of the shock parameters at the field lines suggests that the release of the SEPs is observed around the time when the wave steepens into a shock wave or when the shock wave becomes supercritical. Electron release times at SolO and STEREO-A are consistent with the onset times of the supercritical shock and occur when the shock is transitioning between quasi-perpendicular to oblique geometry. The release times of energetic protons at the two locations are significantly delayed with respect to when the shock becomes supercritical and occur when the shock is quasi-parallel, which adds considerable complexity to the analysis.

Overall, the delays of the SEP release times relative to the time that the pressure wave connects to a spacecraft could be attributed to the time that the wave takes to steepen into a shock. Efficient acceleration of particles at the wavefront and release to the field lines connected to the spacecraft is not possible before the pressure wave steepens into a shock. Additionally, the acceleration efficiency dramatically increases when the shock wave becomes supercritical. Electrons can easily be reflected in shock waves with any magnetic compression, even if the shock is not supercritical. However, this does not apply to protons and this could be an important difference in the observed delays between the two species. When the shock wave progressively becomes supercritical along the field lines, the injection of the protons into the acceleration process starts to be very efficient. The shock geometry could also have an additional role to the delays, as the acceleration efficiency of the different species depends on this parameter. For example, thermal protons are accelerated more efficiently at quasi-parallel shocks and energetic electrons at quasi-perpendicular shock conditions. Therefore, depending on the shock strength and geometry, it is expected that the acceleration and release timescales of energetic electrons will be different from those of protons. The present analysis and the uncertainties in the modelling and data do not permit us to propose a single scenario able to explain the delayed release of protons at large angular distances in this event. This question needs to be analysed when more events observed by widely separated spacecraft become available, hopefully also from distances close to the Sun where uncertainties in the transport pose less of a problem. This is because a significant part of these delays could be attributed to the prolongation of the path length travelled by energetic protons before their detection compared to that of electrons, as discussed by Kollhoff et al. (2021). This prolongation can be caused by the meandering of field lines (e.g., Laitinen & Dalla 2019), by intervening structures existing in the interplanetary medium, or by limitations of the VDA and TSA methods that are commonly used to estimate the SEP release times (Lintunen & Vainio 2004; Vainio et al. 2013) and are possibly responsible for the estimated time delays (Laitinen et al. 2015).

The last aspect of our analysis is the role of the shock wave for the energetic particles observed near Earth. As explained above, the shock modelling at this location is a difficult task and may contain significant uncertainties. However, we find that a very weak (and subcritical) shock wave could have formed near the region where Earth is presumably connected. Once a CME-driven shock is decoupled from the CME, the shock wave should convert into a decaying shock wave that will evolve into a linear wave over the distance (Kwon & Vourlidas 2017, 2018). In this regard, the SEPs observed at Earth may mainly result from cross-field transport processes of particles accelerated in the stronger shock parts near the Earth magnetic field line. This is consistent with the delayed SEP onset times at Earth and also the low values of the first-order anisotropy. As the low anisotropy can also be caused by very strong scattering in the interplanetary space, further studies might be necessary to confirm whether cross-field diffusion is behind the particles arriving at Earth.

6. Conclusion

Our key findings can be summarised as follows:

- We show evidence that the shock wave could play an important role in the wide spread of SEPs observed on 2020 November 29. Supercritical shock regions are connected to most of the observers where efficient shock acceleration is expected to take place.
- The EUV wave weakens low in the low corona towards the field lines magnetically connected to the distant spacecraft. This probably makes it difficult for the shock to contribute to the SEP acceleration and release at low coronal heights. The shock wave expands rapidly in the high corona and probably contributes to the SEP release for most of the observers.
- We show that Earth barely connects to a shock wave; therefore cross-field transport could have a dominant role in the particle increase at this location.
- The SEP release times do not show any specific ordering with thresholds of the shock strength or the shock geometry. The release time of energetic electrons seems to occur close to the time that the shock wave connects to or becomes supercritical at the field lines connecting to the spacecraft. The release time of energetic protons is delayed relative to the time that the shock strength becomes maximum or reaches a plateau.

This study of the first widespread SEP event of solar cycle 25 on 2020 November 29 demonstrates the importance of data-driven shock wave reconstruction, 3D modelling, and magnetic connectivity analysis to help understand the role of shock waves in accelerating and transporting particles in widespread SEP events. Nevertheless, there remain open questions that need to be solved. This study demonstrates that observations from PSP and SolO will be crucial to improving our understanding of particle acceleration and transport in the inner heliosphere. The models can also benefit from the data that will be obtained by the two new missions and especially by Solar Orbiter, where there will be a particular focus on the comparison between remote sensing and in situ data. As the new solar cycle 25 builds up and the solar activity increases, we expect that more SEP events will be observed with various characteristics.

Acknowledgements. The authors thank an anonymous referee for a detailed review that improved the quality of the manuscript. This study has received funding from the European Union's Horizon 2020 research and innovation programme under grant agreement No. 101004159 (SERPENTINE) and No. 870405 (EUHFORIA 2.0). A.K. and A.P.R. acknowledge financial support from the ANR COROSHOCK (ANR-17-CE31-0006-01). R-YK acknowledges support from the National Research Foundation of Korea (NRF-2019R1F1A1062079) grant funded by the Korea government (MSIT; Project No. 2019-2-850-09). L.R-G. is supported by the European Space Agency under the ESA/NPI program and acknowledges the additional financial support by the Spanish Ministerio de Ciencia, Innovación y Universidades FEDER/MCIU/AEI Projects ESP2017-88436-R and PID2019-104863RB-I00/AEI/10.13039/501100011033. She also thanks Laura Balmaceda, Teresa Nieves-Chinchilla, Leila Mays, and Dusan Odstrcil for their help. D.L.

acknowledges support from NASA Living With a Star (LWS) programs NNH17ZDA001N-LWS and NNH19ZDA001N-LWS, the Goddard Space Flight Center Internal Scientist Funding Model (competitive work package) program and the Heliophysics Innovation Fund (HIF) program. N.D. is grateful for support by the Turku Collegium for Science, Medicine and Technology of the University of Turku, Finland. The IRAP team acknowledges support from the French space agency (Centre National des Etudes Spatiales; CNES; `https://cnes.fr/fr`) that funds activity in plasma physics data center (Centre de Données de la Physique des Plasmas; CDPP; `http://cdpp.eu/`) and the Multi Experiment Data & Operation Center (MEDOC; `https://idoc.ias.u-psud.fr/MEDOC`), and the space weather team in Toulouse (Solar-Terrestrial Observations and Modelling Service; STORMS; `http://stormsweb.irap.omp.eu/`). R.V. acknowledges the support of the Academy of Finland (grant nr. 336809). C.D., J.A.L., P.R., and T.T. were supported by NASA's HTMS and HSO-C programmes (Grant Nos. 80NSSC20K1274 and 80NSSC20K1285, respectively) and NSF's PREEVENTS program (Grant No. ICER-1854790). We thank the STEREO: SECCHI SOHO: LASCO; SDO/AIA teams and Predictive Science Inc. for providing the data used in this study. The STEREO SECCHI data are produced by a consortium of RAL (UK), NRL (USA), LMSAL (USA), GSFC (USA), MPS (Germany), CSL (Belgium), IOTA (France) and IAS (France). SOHO is a mission of international cooperation between ESA and NASA. The SDO/AIA data used are courtesy of SDO (NASA) and the AIA consortium. Some data processing for this research was carried out using version 3.0.1 (Mumford et al. 2021) of the SunPy open source software package (SunPy Community 2020). ENLIL simulation results have been provided by the CCMC at NASA Goddard Space Flight Center (GSFC) through their public Runs on Request system (`http://ccmc.gsfc.nasa.gov`; run ID Laura_Rodriguez-Garcia_051121_SH_1). The WSA model was developed by N. Arge, currently at GSFC, and the ENLIL Model was developed by D. Odstrcil, currently at George Mason University.

References

Acuña, M. H., Curtis, D., Scheifele, J. L., et al. 2008, Space Sci. Rev., 136, 203
Afanasiev, A., Vainio, R., Rouillard, A. P., et al. 2018, A&A, 614, A4
Anastasiadis, A., Lario, D., Papaioannou, A., et al. 2019, Phil. Trans. R. Soc. London, Ser. A, 377, 20180100
Arge, C. N., & Pizzo, V. J. 2000, J. Geophys. Res., 105, 10465
Arge, C. N., Henney, C. J., Koller, J., et al. 2010, Twelfth International Solar Wind Conference, 1216, 343
Arge, C. N., Henney, C. J., Hernandez, I. G., et al. 2013, Sol. Wind, 13, 11
Bale, S. D., Goetz, K., Harvey, P. R., et al. 2016, Space Sci. Rev., 204, 49
Brueckner, G. E., Howard, R. A., Koomen, M. J., et al. 1995, Sol. Phys., 162, 357
Cohen, C. M. S., Christian, E. R., Cummings, A. C., et al. 2021, A&A, 656, A29
Dalla, S., Balogh, A., Krucker, S., et al. 2003, Geophys. Res. Lett., 30, 8035
Desai, M., & Giacalone, J. 2016, Liv. Rev. Sol. Phys., 13, 3
Downs, C., Lionello, R., Mikić, Z., et al. 2016, ApJ, 832, 180
Downs, C., Warmuth, A., Long, D. M., et al. 2021, ApJ, 911, 118
Dresing, N., Gómez-Herrero, R., Klassen, A., et al. 2012, Sol. Phys., 281, 281
Dresing, N., Gómez-Herrero, R., Heber, B., et al. 2014, A&A, 567, A27
Dröge, W., Kartavykh, Y. Y., Klecker, B., et al. 2010, ApJ, 709, 912
Dumbović, M., Guo, J., Temmer, M., et al. 2019, ApJ, 880, 18
Fox, N. J., Velli, M. C., Bale, S. D., et al. 2016, Space Sci. Rev., 204, 7
Galvin, A. B., Kistler, L. M., Popecki, M. A., et al. 2008, Space Sci. Rev., 136, 437
Giacalone, J., & Jokipii, J. R. 2004, ApJ, 616, 573
Giacalone, J., Burgess, D., Bale, S.D., et al. 2021, ApJ, in press
Gómez-Herrero, R., Dresing, N., Klassen, A., et al. 2015, ApJ, 799, 55
Gopalswamy, N., Akiyama, S., Yashiro, S., et al. 2015a, ArXiv e-prints [arXiv:`1508.01603`]
Gopalswamy, N., Mäkelä, P., Yashiro, S., et al. 2015b, J. Phys. Conf. Ser., 642, 012012
Hapgood, M. A. 1992, Planet. Space Sci., 40, 711
Harvey, J. W., Hill, F., Hubbard, R. P., et al. 1996, Science, 272, 1284
Horbury, T. S., O'Brien, H., Carrasco Blazquez, I., et al. 2020, A&A, 642, A9
Howard, R. A., Moses, J. D., Vourlidas, A., et al. 2008, Space Sci. Rev., 136, 67
Hu, H., Liu, Y. D., Zhu, B., et al. 2019, ApJ, 878, 106
Kaiser, M. L., Kucera, T. A., Davila, J. M., et al. 2008, Space Sci. Rev., 136, 5
Klein, K.-L., & Dalla, S. 2017, Space Sci. Rev., 212, 1107
Kollhoff, A., Kouloumvakos, A., Lario, D., et al. 2021, A&A, 656, A20
Kouloumvakos, A., Nindos, A., Valtonen, E., et al. 2015, A&A, 580, A80
Kouloumvakos, A., Patsourakos, S., Nindos, A., et al. 2016, ApJ, 821, 31
Kouloumvakos, A., Rouillard, A. P., Wu, Y., et al. 2019, ApJ, 876, 80
Kouloumvakos, A., Vourlidas, A., Rouillard, A. P., et al. 2020a, ApJ, 899, 107
Kouloumvakos, A., Rouillard, A. P., Share, G. H., et al. 2020b, ApJ, 893, 76
Kouloumvakos, A., Rouillard, A., Warmuth, A., et al. 2021, ApJ, 913, 99
Kozarev, K. A., Raymond, J. C., Lobzin, V. V., et al. 2015, ApJ, 799, 167
Kwon, R.-Y., & Vourlidas, A. 2017, ApJ, 836, 246
Kwon, R.-Y., & Vourlidas, A. 2018, J. Space Weather Space Clim., 8, A08
Kwon, R.-Y., Ofman, L., Olmedo, O., et al. 2013, ApJ, 766, 55
Kwon, R.-Y., Zhang, J., & Olmedo, O. 2014, ApJ, 794, 148
Kwon, R.-Y., Zhang, J., & Vourlidas, A. 2015, ApJ, 799, L29
Laitinen, T., & Dalla, S. 2019, ApJ, 887, 222
Laitinen, T., Dalla, S., & Marsh, M. S. 2013, ApJ, 773, L29
Laitinen, T., Huttunen-Heikinmaa, K., Valtonen, E., et al. 2015, ApJ, 806, 114
Laitinen, T., Kopp, A., Effenberger, F., et al. 2016, A&A, 591, A18
Lario, D., Raouafi, N. E., Kwon, R.-Y., et al. 2014, ApJ, 797, 8
Lario, D., Kwon, R.-Y., Vourlidas, A., et al. 2016, ApJ, 819, 72
Lario, D., Kwon, R.-Y., Richardson, I. G., et al. 2017a, ApJ, 838, 51
Lario, D., Kwon, R.-Y., Riley, P., & Raouafi, N. E. 2017b, ApJ, 847, 103
Lario, D., Richardson, I. G., Palmerio, E., et al. 2021, ApJ, 920, 123
Lemen, J. R., Title, A. M., Akin, D. J., et al. 2012, Sol. Phys., 275, 17
Lintunen, J., & Vainio, R. 2004, A&A, 420, 343
Lionello, R., Linker, J. A., & Mikić, Z. 2009, ApJ, 690, 902
Long, D. M., DeLuca, E. E., & Gallagher, P. T. 2011, ApJ, 741, L21
Long, D. M., Bloomfield, D. S., Chen, P. F., et al. 2017, Sol. Phys., 292, 7
Malandraki, O. E., Marsden, R. G., Lario, D., et al. 2009, ApJ, 704, 469
Mann, G., Klassen, A., Aurass, H., et al. 2003, A&A, 400, 329
Mann, G., Melnik, V. N., Rucker, H. O., et al. 2018, A&A, 609, A41
Mason, G. M., Cohen, C. M. S., Ho, G. C., et al. 2021, A&A, 656, L12
Mikić, Z., Downs, C., Linker, J. A., et al. 2018, Nat. Astron., 2, 913
Mitchell, J. G., De Nolfo, G. A., Hill, M. E., et al. 2021, ApJ, 919, 119
Miteva, R., Klein, K.-L., Kienreich, I., et al. 2014, Sol. Phys., 289, 2601
Müller, D., St. Cyr, O. C., Zouganelis, I., et al. 2020, A&A, 642, A1
Mumford, S. J., Freij, N., Christe, S., et al. 2021, `https://doi.org/10.5281/zenodo.5068086`
Nandy, D. 2021, Sol. Phys., 296, 54
Nieves-Chinchilla, T., Alzate, N., Cremades, H., et al. 2022, ApJ, submitted [arXiv:`2201.11212`]
Nolte, J. T., & Roelof, E. C. 1973, Sol. Phys., 33, 241
Odstrcil, D. 2003, Adv. Space Res., 32, 497
Odstrčil, D., Dryer, M., & Smith, Z. 1996, J. Geophys. Res., 101, 19973
Olmedo, O., Vourlidas, A., Zhang, J., et al. 2012, ApJ, 756, 143
Ontiveros, V., & Vourlidas, A. 2009, ApJ, 693, 267
Paassilta, M., Papaioannou, A., Dresing, N., et al. 2018, Sol. Phys., 293, 70
Park, J., Innes, D. E., Bucik, R., et al. 2013, ApJ, 779, 184
Patsourakos, S., & Vourlidas, A. 2012, Sol. Phys., 281, 187
Patsourakos, S., Vourlidas, A., Wang, Y. M., et al. 2009, Sol. Phys., 259, 49
Plotnikov, I., Rouillard, A. P., & Share, G. H. 2017, A&A, 608, A43
Poirier, N., Rouillard, A. P., Kouloumvakos, A., et al. 2021, Front. Astron. Space Sci., 8, 684734
Prise, A. J., Harra, L. K., Matthews, S. A., et al. 2014, Sol. Phys., 289, 1731
Reames, D. V. 2015, Space Sci. Rev., 194, 303
Richardson, I. G., von Rosenvinge, T. T., Cane, H. V., et al. 2014, Sol. Phys., 289, 3059
Riley, P., Lionello, R., Linker, J. A., et al. 2011, Sol. Phys., 274, 361
Rodríguez-García, L., Gómez-Herrero, R., Zouganelis, I., et al. 2021, A&A, 653, A137
Rouillard, A. P., Sheeley, N. R., Tylka, A., et al. 2012, ApJ, 752, 44
Rouillard, A. P., Plotnikov, I., Pinto, R. F., et al. 2016, ApJ, 833, 45
Rouillard, A. P., Pinto, R. F., Vourlidas, A., et al. 2020, A&A, 642, A2
Schatten, K. H., Wilcox, J. M., & Ness, N. F. 1969, Sol. Phys., 6, 442
Schrijver, C. J., & De Rosa, M. L. 2003, Sol. Phys., 212, 165
Sheeley, N. R., Hakala, W. N., & Wang, Y.-M. 2000, J. Geophys. Res., 105, 5081
Stenborg, G., Vourlidas, A., & Howard, R. A. 2008, ApJ, 674, 1201
SunPy Community, Barnes, W. T., Bobra, M. G., et al., 2020, ApJ, 890, 68
Thernisien, A. 2011, ApJS, 194, 33
Thernisien, A. F. R., Howard, R. A., & Vourlidas, A. 2006, ApJ, 652, 763
Torsti, J., Kocharov, L. G., Teittinen, M., et al. 1999, ApJ, 510, 460
Vainio, R., Valtonen, E., Heber, B., et al. 2013, J. Space Weather Space Clim., 3, A12
Vlahos, L., Anastasiadis, A., Papaioannou, A., et al. 2019, Phil. Trans. R. Soc. London Ser. A, 377, 20180095
Vourlidas, A., Wu, S. T., Wang, A. H., et al. 2003, ApJ, 598, 1392
Warmuth, A. 2015, Liv. Rev. Sol. Phys., 12, 3
Warmuth, A., & Mann, G. 2005, A&A, 435, 1123
Webb, D. F., & Howard, T. A. 2012, Liv. Rev. Sol. Phys., 9, 3
Worden, J., & Harvey, J. 2000, Sol. Phys., 195, 247
Zhang, J., Temmer, M., Gopalswamy, N., et al. 2021, Prog. Earth Planet. Sci., 8, 56
Zhu, B., Liu, Y. D., Kwon, R.-Y., et al. 2018, ApJ, 865, 138
Zucca, P., Morosan, D. E., Rouillard, A. P., et al. 2018, A&A, 615, A89

Appendix A: Temporal evolution of the shock parameters

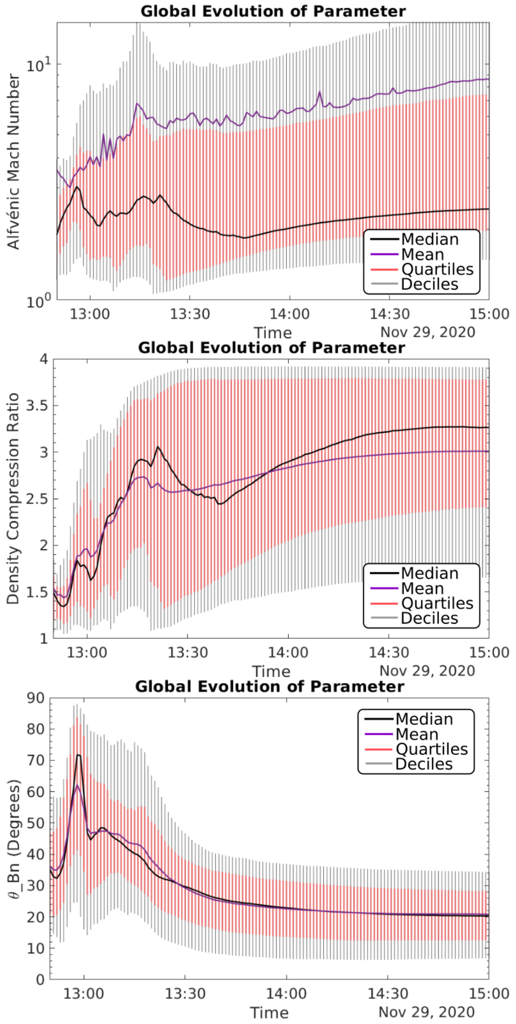

Fig. A.1. Temporal evolution of the $\mathrm{M_A}$ (top panel), X (middle panel), and θ_{BN} (bottom panel) obtained from the shock wave modelling. The time-varying distribution characteristics of the shock parameters are presented in each panel. The median values are depicted with the black lines, the mean with purple lines, and the first and third quartile and the first and ninth decile values are indicated with the red and grey vertical bars, respectively.

For each of the shock parameters we calculated the time-varying distribution characteristics (mean, median, first and third quartile, and first and ninth decile values) considering the entire surface and only regions where a shock wave was probably formed ($X > 1$). In Fig. A.1 we show the temporal evolution of the shock parameters as obtained from the 3D modelling for the regions where $X > 1$. From the temporal evolution of the M_A and X, we see that there are regions where a shock wave has formed from the start of the shock modelling. We find that the median M_A values vary from around two to three during the full modelling interval. The median compression ratio starts from around 1.5 and progressively increases to around 3.2 near the end of the modelling. The shock geometry starts from oblique and changes rapidly to quasi-perpendicular, with median θ_{BN} values starting from ~35° and increasing to 70° until 12:58 UT. At this time there is a maximum of θ_{BN} and afterwards, the θ_{BN} changes rapidly towards quasi-parallel and reaches a lower plateau after 13:45 UT with median θ_{BN} values near 20°.

Appendix B: Details of the WSA-ENLIL modelling

Table B.1. The CME reconstruction parameters from the GCS model.

CME#	Date[b] [UT]	Long.[a] [°]	Lat.[a] [°]	Tilt [°]	Width[c] [°]	Speed[d] [km/s]
CME1	11/24 04:36	-67	-23	-21	47	820
CME2	11/24 13:25	-153	-10	-12	100	1141
CME3	11/26 21:24	-102	8	-60	36	576
CME4	11/29 13:25	-83	-15	-70	74	1780

Notes. [a] The longitude and latitude values are given in the HGS coordinate system. [b] The date and time is determined by the first appearance of the CMEs on SOHO/LASCO/C2 coronagraphs. [c] The CME width is based on Dumbović et al. (2019). It is the angular extent in the equatorial plane taking the CME tilt into account. [d] The speed at the CME's leading edge.

The WSA-ENLIL model is a global 3D MHD model that generates a time-dependent background characterisation of the heliosphere outside of 21.5 $R_\odot$. The model simulates the solar wind and the evolution of superimposed CME structures from about 0.1 au to 1 au and beyond. The inner boundary condition is given by the WSA V5.2 model, which uses standard quick-reduce zero-point corrected magnetograms from the Global Oscillations Network Group (GONG, Harvey et al. 1996), available from the National Solar Observatory website[8]. As an output of this heliosphere characterisation, ENLIL gives an estimation of the magnetic connectivity of the different spacecraft at 21.5 $R_\odot$. However, the ENLIL model has some limitations because it does not include an internal magnetic field within the CMEs, and hence the simulated magnetic field may not be fully adequate.

In order to obtain an overall overview of the heliospheric context where the SEP event on 2020 November 29 occurred, we performed a WSA-ENLIL+Cone simulation, including the CMEs observed prior to this event. We used the GCS model to reconstruct the injected CMEs. Three CMEs were observed prior to the SEP event and are relevant to the estimates of the magnetic connections, two were observed on 2020 November 24 at 04:35 UT (CME1) and 13:25 UT[9] (CME2), respectively, and one on 2020 November 26 at 21:24 UT (CME3). Table B.1 provides the parameters obtained from the GCS model for these three CMEs as well as for the CME on 2020 November 29 that generated the SEP event under study (CME4). The fastest and widest among the three prior CMEs was the CME2, with a speed at the leading edge of 1141 km s^{-1} and width of 100°. The central direction of propagation for CME2 was in the space between PSP and SolO at an HGS longitude of ~153° and it was not observed in situ. CME3 was observed by PSP in situ before the arrival of the shock and ICME of the November 29 event.

Figure B.1 shows the comparison between the in situ data and, over-plotted in pink line, the result of the ENLIL simulation at the locations of SolO (Fig. B.1a), PSP (Fig. B.1b), STEREO-A (Fig. B.1c) and Earth (Fig. B.1d). From top to bottom, the four plots include the magnetic field strength, the magnetic field latitudinal and azimuthal angles, θ_{B-RTN} and ϕ_{B-RTN}, solar wind proton speed and density. The

---

[8] `ftp://gong2.nso.edu/QR/zqs/`

[9] Time of the CMEs first appearance on SOHO/LASCO coronagraphs

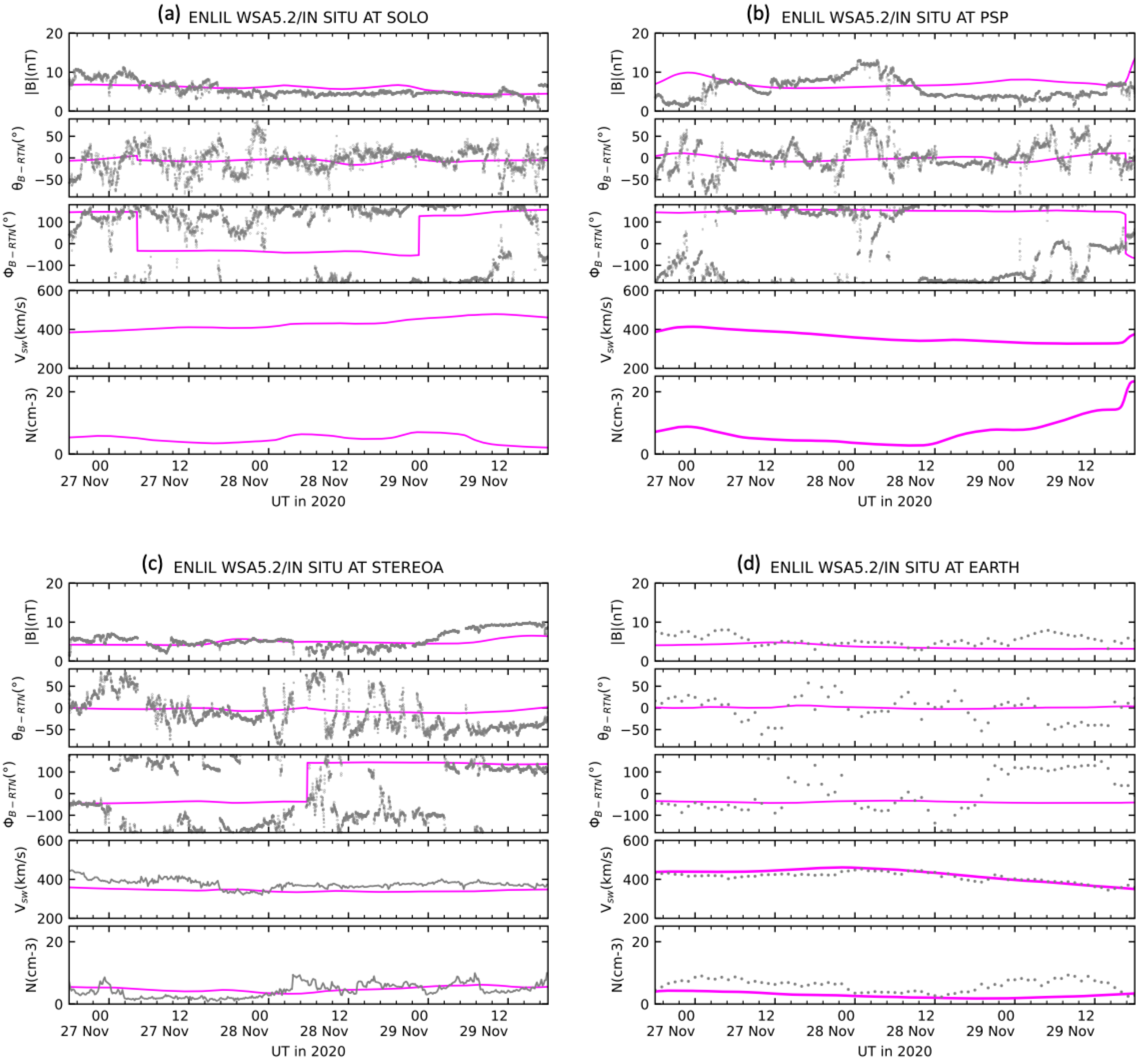

Fig. B.1. In situ observations at the locations of SolO (a), PSP (b), STEREO-A (c), and Earth (d) over-plotted with the ENLIL results (pink line) for the three days prior to the estimated SEP release time. *From top to bottom*, the panels show magnetic field strength, the magnetic field latitudinal and azimuthal angles, θ_{B-RTN} and ϕ_{B-RTN}, and solar wind proton speed and density.

one-minute-averaged magnetic field observations are from the magnetometer instrument (MAG, Horbury et al. 2020) on board SolO (a) and from the FIELDS instrument on board PSP (b). One-minute-averaged magnetic field and ten-minute-averaged solar wind plasma data are from the Magnetic Field Experiment (Acuña et al. 2008) and from the Plasma and Suprathermal Ion Composition (PLASTIC, Galvin et al. 2008) investigation on board STEREO-A (c), respectively. One-hour-averaged magnetic field and solar wind plasma data at Earth are from Near-Earth Heliosphere Data (OMNI)[10] (d). At the locations of STEREO-A and Earth, where there is solar wind plasma data available, Figure B.1c and d shows that ENLIL speed follows the general trend and magnitude of the observed solar wind speed (fourth panel).

---

[10] `https://omniweb.gsfc.nasa.gov/coho/html/cw_data.html`